Published for SISSA by Springer

Received: *April 5, 2025*
Accepted: *June 28, 2025*
Published: *August 13, 2025*

# Production of protons, deuterons and tritons in argon-nucleus interactions at 3.2 A GeV


## The BM@N collaboration

S. Afanasiev[a], G. Agakishiev[a], A. Aleksandrov[i], E. Aleksandrov[a], I. Aleksandrov[a], P. Alekseev[a,c], K. Alishina[a], V. Astakhov[a], T. Aushev[e], V. Azorskiy[a], V. Babkin[a], N. Balashov[a], R. Barak[a], A. Baranov[h], D. Baranov[a], N. Baranova[h], N. Barbashina[f], S. Bazylev[a], M. Belov[d], D. Blau[c], V. Bocharnikov[g], G. Bogdanova[h], E. Bondar[l], E. Boos[h], E. Bozorov[m], M. Buryakov[a], S. Buzin[a], A. Chebotov[a], D. Chemezov[a], J.H. Chen[k], A. Demanov[a,f], D. Dementev[a], A. Dmitriev[a], J. Drnoyan[a], D. Dryablov[a], B. Dubinchik,[a] P. Dulov[a,j], A. Egorov[a], D. Egorov[a], V. Elsha[a], A. Fediunin[a], A. Fedosimova[l], I. Filippov[a], I. Filozova[a], D. Finogeev[b], I. Gabdrakhmanov[a], O. Gavrischuk[a], K. Gertsenberger[a], O. Golosov[f], V. Golovatyuk[a], P. Grigoriev[a], M. Golubeva[b], F. Guber[b], S. Ibraimova[l], D. Idrisov[b], T. Idrissova[l], A. Ivashkin[b], A. Izvestnyy[b], V. Kabadzhov[j], A. Kakhorova[m], Sh. Kanokova[m], M. Kapishin[a], I. Kapitonov,[a] V. Karjavin[a], D. Karmanov[h], N. Karpushkin[a,b], R. Kattabekov[a], V. Kekelidze[a], S. Khabarov[a], P. Kharlamov[a,h], G. Khudaiberdyev[m], A. Khvorostukhin,[a] V. Kireyeu[a], Yu. Kiryushin[a], P. Klimai[b,e], V. Kolesnikov[a], A. Kolozhvari[a], Yu. Kopylov[a], M. Korolev[h], L. Kovachev[a,n], I. Kovalev[h], Yu. Kovalev,[a] V. Kozlov[d], I. Kruglova[a], S. Kuklin[a], E. Kulish[a], A. Kurganov[h], V. Kutergina[a], A. Kuznetsov[a], E. Ladygin[a], D. Lanskoy[h], N. Lashmanov[a], I. Lebedev[l], V. Lenivenko[a], R. Lednicky[a], V. Leontiev[a,h], E. Litvinenko[a], D. Lyapin[b], Y.G. Ma[k], A. Makankin[a], A. Makhnev[b], A. Malakhov[a], M. Mamaev[a,f], A. Martemianov[c], M. Merkin[h], S. Merts[a], S. Morozov[a,b], Yu. Murin[a], K. Musaev[m], G. Musulmanbekov[a], D. Myktybekov[l], R. Nagdasev[a], S. Nemnyugin[i], D. Nikitin[a], R. Nizamov[i], S. Novozhilov[a], A. Olimov[m], Kh. Olimov[m], K. Olimov[m], V. Palichik[a], P. Parfenov[a,f], I. Pelevanyuk[a], D. Peresunko[c], S. Piyadin[a], M. Platonova[h], V. Plotnikov[a], D. Podgainy[a], I. Pshenichnov[b], N. Pukhaeva,[a] F. Ratnikov[g], S. Reshetova[a], V. Rogov[a], I. Romanov[a], I. Rufanov[a], P. Rukoyatkin[a], M. Rumyantsev[a],



https://doi.org/10.1007/JHEP08(2025)095

JHEP08(2025)095

**T. Rybakov**[c], **D. Sakulin**[a], **S. Savenkov**[b], **D. Serebryakov**[b], **A. Shabanov**[b], **S. Sergeev**[a], **A. Serikkanov**[l], **A. Sheremetev**[a], **A. Sheremeteva**[a], **A. Shchipunov**[a], **M. Shitenkov**[a], **M. Shodmonov**[m], **M. Shopova**[j], **A. Shutov**[a], **V. Shutov**[a], **I. Slepnev**[a], **V. Slepnev**[a], **I. Slepov**[a], **A. Smirnov**[a], **A. Solomin**[h], **A. Sorin**[a], **V. Spaskov**[a], **A. Stavinskiy**[a,c], **V. Stekhanov**[c], **Yu. Stepanenko**[a], **E. Streletskaya**[a], **O. Streltsova**[a], **M. Strikhanov**[f], **E. Sukhov**[a], **D. Suvarieva**[a,j], **A. Svetlichnyi**[b], **G. Taer**[c], **A. Taranenko**[a,f], **N. Tarasov**[a], **O. Tarasov**[a], **P. Teremkov**[d], **A. Terletsky**[a], **O. Teryaev**[a], **V. Tcholakov**[j], **V. Tikhomirov**[a], **A. Timoshenko**[a], **O. Tojiboev**[m], **N. Topilin**[a], **T. Tretyakova**[h], **V. Troshin**[a,f], **A. Truttse**[f], **I. Tserruya**[o], **V. Tskhay**[d], **I. Tyapkin**[a], **V. Ustinov**[a], **V. Vasendina**[a], **V. Velichkov**[a], **V. Volkov**[b], **A. Voronin**[h], **A. Voronin**[a], **N. Voytishin**[a], **B. Yuldashev**[m], **V. Yurevich**[a], **N. Zamiatin**[a], **M. Zavertyaev**[d], **S. Zhang**[k], **I. Zhavoronkova**[a,f], **N. Zhigareva**[c], **A. Zinchenko**[a], **R. Zinchenko**[a], **A. Zubankov**[b], **E. Zubarev**[a] and **M. Zuev**[a]

[a] *Joint Institute for Nuclear Research (JINR), Dubna, Russia*
[b] *Institute for Nuclear Research of the RAS (INR RAS), Moscow, Russia*
[c] *Kurchatov Institute, NRC, Moscow, Russia*
[d] *Lebedev Physical Institute of the Russian Academy of Sciences (LPI RAS), Moscow, Russia*
[e] *Moscow Institute of Physics and Technology (MIPT), Moscow, Russia*
[f] *National Research Nuclear University MEPhI, Moscow, Russia*
[g] *National Research University Higher School of Economics (HSE University), Moscow, Russia*
[h] *Skobeltsyn Institute of Nuclear Physics, Moscow State University (SINP MSU), Moscow, Russia*
[i] *St Petersburg University (SPbU), St Petersburg, Russia*
[j] *Plovdiv University "Paisii Hilendarski", Plovdiv, Bulgaria*
[k] *Key Laboratory of Nuclear Physics and Ion-Beam Application (MOE), Institute of Modern Physics, Fudan University, Shanghai, China*
[l] *Institute of Physics and Technology, Satbayev University, Almaty, Kazakhstan*
[m] *Physical-Technical Institute of Uzbekistan Academy of Sciences (PhTI of UzAS), Tashkent, Uzbekistan*
[n] *Institute of Mechanics at the Bulgarian Academy of Sciences (IMech-BAS), Sofia, Bulgaria*
[o] *Weizmann Institute of Science, Rehovot, Israel*

*E-mail:* bmn@jinr.ru

Abstract: Results of the BM@N experiment at the Nuclotron/NICA complex on the production of protons, deuterons and tritons in interactions of an argon beam of 3.2 A GeV with fixed targets of C, Al, Cu, Sn and Pb are presented. Transverse mass spectra, rapidity distributions and multiplicities of protons, deuterons and tritons are measured. The results are treated within a coalescence approach and compared with predictions of theoretical models and with other measurements.

Keywords: Heavy Ion Experiments, Minimum Bias

ArXiv ePrint: 2504.02759

JHEP08(2025)095

## Contents



JHEP08(2025)095

## 1 Introduction

BM@N (Baryonic Matter at Nuclotron) is the first operational experiment at the Nuclotron/NICA accelerator complex. The Nuclotron provides beams of a variety of particles, from protons up to gold ions, with kinetic energy in the range from 1 to 6 A GeV for light ions with Z/A ratio of $\sim$0.5 and up to 4.5 A GeV for heavy ions with Z/A ratio of $\sim$0.4. At these energies, the nucleon density in the fireball created in collisions of heavy ions with fixed targets is 3–4 times higher than the nuclear saturation density [1], thus allowing one to study heavy-ion interactions in the high-density baryonic matter regime [2–5].

During the commissioning phase, BM@N, in a configuration with limited phase-space coverage, collected its first data with beams of carbon, argon and krypton ions [6, 7]. In the first physics publication, BM@N reported studies of $\pi^+$ and $K^+$ production in argon-nucleus interactions [8]. This paper presents results on proton, deuteron and triton production in 3.2 A GeV argon-nucleus interactions.

At the Nuclotron energies, baryon transfer over finite rapidity distances (baryon stopping [9]) plays an important role [10]–[12]. The baryon density achieved in high-energy nuclear collisions is a crucial quantity that governs the reaction dynamics and the overall system evolution, including eventual phase transitions. The baryon rapidity distributions in heavy ion collisions for different combinations of projectile and target as well as at different impact parameters provide essential constraints on the dynamical scenarios of baryon stopping. The BM@N experimental setup allows for the measurement of the distribution of protons and light nuclei $(d, t)$ over the rapidity interval [1.0–2.2]. This rapidity range is wide enough to include not only the midrapidity (rapidity of the nucleon-nucleon center-of-mass (CM)

system is $y_{\mathrm{CM}} = 1.08$) but also the beam rapidity region ($y_{\mathrm{beam}} = 2.16$), in contrast to the collider experiments focused mainly on in the mid-rapidity region. Another advantage of BM@N consists in the coverage of a wide interval of transverse momenta ($p_T$) of produced nuclear clusters (light nuclei). This makes possible to determine the general shape of the rapidity density distribution and derive information about the rapidity shift and energy loss in nucleus-nucleus collisions.

Nuclear cluster production allows one to estimate the nucleon phase-space density attained in the reaction [13]. It governs the overall evolution of the reaction process and may provide information about freeze-out conditions and entropy production in relativistic nucleus-nucleus interactions. The nucleon phase space density can be obtained from the ratio of deuteron and proton abundances. One of the goals of this work is to study the particle phase-space density evolution in Ar+A collisions for different projectile-target combinations and as a function of collision centrality.

In collisions of heavy nuclei at relativistic energies, a significant fraction of the initial kinetic energy transforms into particle production and thermal excitation of matter. Various dynamical models, including those based on hydrodynamics, have demonstrated that the entropy per baryon $S/A$ created during the initial interaction stage remains constant during the subsequent evolution of the system [16, 17]. Therefore, entropy production data provide insight not only into the nucleon phase-space density at the final stage of the reaction (freeze-out), but also into the properties of the medium during the hot and dense stage. It is also the aim of this work to investigate the entropy evolution in the reaction zone with system size in argon-nucleus collisions and compare BM@N results with results of other experiments.

The few MeV binding energies of the deuteron and the triton are much lower than the freeze-out temperatures estimated to be above 100 MeV. These light clusters are therefore not expected to survive through the high density stages of the collision. The deuterons and tritons observed in the experiment are emitted at the end of the freeze-out process, carrying information about this late stage of the collision.

Light cluster production in low-energy heavy-ion collisions is well described by a simple coalescence model [18–21] based on the distributions of their constituents (protons and neutrons) and a coalescence parameter $B_A$ related to the cluster mass number A. In order to describe heavy-ion collisions at high energies, the simple coalescence model has been modified to account for the nucleon phase space distributions at the freeze-out and also for the strength of the momentum-space correlations induced by collective flow [22]. In central heavy-ion collisions, the pressure gradient in the system generates strong transverse radial flow. Therefore, nucleon clusters inside a collective velocity field acquire additional momenta proportional to the masses of these clusters.

The paper is organized as follows: the experimental setup is described in section 2, the event reconstruction is detailed in section 3, and the evaluation of proton, deuteron, and triton reconstruction efficiency is presented in section 4. The methodology to define collision centrality classes is explained in section 5. The evaluation of the cross sections, multiplicities, and systematic uncertainties is addressed in section 6. The transverse mass and rapidity distributions of protons, deuterons, and tritons are presented in section 7. The BM@N results are compared with predictions from the DCM-SMM [23, 24] and PHQMD [25] models. The



JHEP08(2025)095

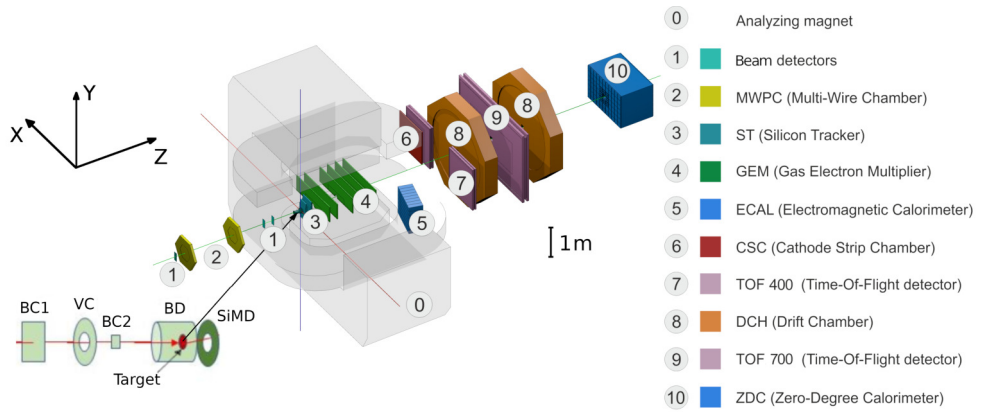


**Figure 1.** Schematic view of the BM@N setup in the argon beam run.

ratios of the transverse momentum distributions of deuterons and tritons to protons are treated within a coalescence approach in section 8. The results are compared with other experimental data on nucleus-nucleus interactions. Results on baryon rapidity loss in argon-nucleus interactions are presented in section 9. The compound ratios of yields of protons and tritons to deuterons are presented in section 10. Finally, a summary is given in section 11.

## 2 Experimental setup

The BM@N detector is a forward spectrometer covering the pseudorapidity range of $1.6 \leq \eta \leq 4.4$. A schematic view of the BM@N setup in the argon-beam run is shown in figure 1. A detailed description of the setup is given in refs. [26, 27]. The spectrometer includes a central tracking system consisting of three planes of forward silicon-strip detectors (ST) and six planes of detectors based on gas electron multipliers (GEM) [28]. The central tracking system is located downstream of the target region inside of a dipole magnet with a bending power of about 2.1 Tm and with a gap of 1.05 m between the poles. In the measurements reported here, the central tracker covered only the upper half of the magnet acceptance.

Two sets of drift chambers (DCH), a cathode strip chamber (CSC), two sets of time-of-flight detectors (ToF), and a zero-degree calorimeter (ZDC) are located downstream of the dipole magnet. The tracking system measures the momenta of charged particles with a relative uncertainty that varies from 2.5% at 0.5 GeV/c to 2% at 1–2 GeV/c and rises linearly to 6.5% at 5 GeV/c. The time resolutions of the time-of-flight systems ToF-400 [29, 30] and ToF-700 [31] are 84 ps and 115 ps, respectively [32].

Two beam counters (BC1, BC2), a veto counter (VC), a barrel detector (BD), and a silicon multiplicity detector (SiMD) are used for event triggering and for the measurement of the incoming beam ions. The BC2 counter also provides the start time T0 for the time-of-flight measurements. The BD detector consists of 40 azimuthal scintillating strips arranged around the target, and the SiMD detector consists of 60 azimuthal silicon segments situated behind the target.

Data were collected with the argon beam with the intensity of a few $10^5$ ions per spill and a spill duration of 2–2.5 s. The kinetic energy of the beam was 3.2 A GeV with a spread of about 1%. A set of solid targets of various materials (C, Al, Cu, Sn and Pb) with an



JHEP08(2025)095

interaction length of 3% was used. The following values of integrated luminosity were achieved for specific targets: 2.1 $\mu b^{-1}$ (C), 2.3 $\mu b^{-1}$ (Al), 1.8 $\mu b^{-1}$ (Cu), 1.1 $\mu b^{-1}$ (Sn), 0.5 $\mu b^{-1}$ (Pb), with the total integrated luminosity of 7.8 $\mu b^{-1}$ obtained at the end of data taking. A total of 16.3 M argon-nucleus collisions at 3.2 A GeV were reconstructed.

A logical beam trigger BT = BC1 $\wedge$ $\overline{\text{VC}}$ $\wedge$ BC2 was used to count the number of beam ions passing the target. The following logic conditions were applied to generate the trigger signal: (1) BT $\wedge$ (BD $\geq 3, 4$); (2) BT $\wedge$ (SiMD $\geq 3, 4$); (3) BT $\wedge$ (BD $\geq 2$) $\wedge$ (SiMD $\geq 3$). The trigger conditions were varied to find the optimal ratio between the event rate and the trigger efficiency for each target. The trigger condition (1) was applied to 60% of the data collected with the carbon target. This trigger fraction was gradually decreasing with increasing the atomic weight of the target down to 26% for the Pb target. In contrast, the fraction of data collected with the trigger condition (2) was increasing from 6% for the carbon target up to 34% for the Pb target. The remaining data were collected with the trigger condition (3).

## 3 Event reconstruction

Track reconstruction in the central tracker is based on a "cellular automaton" approach [33, 34] implementing a constrained combinatorial search of track candidates with their subsequent fitting by a Kalman filter to determine the track parameters. These tracks are used to reconstruct primary and secondary vertices as well as global tracks by extrapolation and matching to hits in the downstream detectors (CSC, DCH and ToF).

The primary collision vertex position (PV) is measured with a resolution of 2.4 mm in the X-Y plane perpendicular to the beam direction and 3 mm in the beam direction.

Charged particles (protons, deuterons and tritons) are identified using the measured time of flight $\Delta t$ between T0 and the ToF detectors, the length of the trajectory $\Delta l$, and the momentum $p$ reconstructed in the central tracker. Then the squared mass $M^2$ of the particle is calculated by the formula: $M^2 = p^2((\Delta tc/\Delta l)^2 - 1)$, where $c$ is the speed of light.

The following criteria are required for selecting proton, deuteron and triton candidates:

- Each track has at least four hits in the GEM detectors (six detectors in total) [28]. Hits in the forward silicon detectors are used to reconstruct the track, but no requirements are applied to the number of hits.

- Tracks originate from the primary vertex. The deviation of the reconstructed vertex $Z_{\text{ver}}$ from the nominal target position along the beam direction $Z_0$ is limited to $-3.4\,\text{cm} < Z_{\text{ver}} - Z_0 < 1.7\,\text{cm}$. The upper limit corresponds to $\sim 5.7\sigma$ of the $Z_{\text{ver}}$ spread and cuts off interactions with the trigger detector located 3 cm behind the target. The beam interaction rate with the trigger detector itself is well below 1%, and it was neglected in Monte Carlo modeling of the experimental setup because its contribution was estimated within the modeling uncertainties.

- Distance of closest approach (DCA) of the track to the primary vertex in the X-Y plane at $\text{Z}_{\text{ver}}$ is required to be less than 1 cm, which corresponds to $4\sigma$ of the vertex residual distribution in the X-Y plane.



JHEP08(2025)095

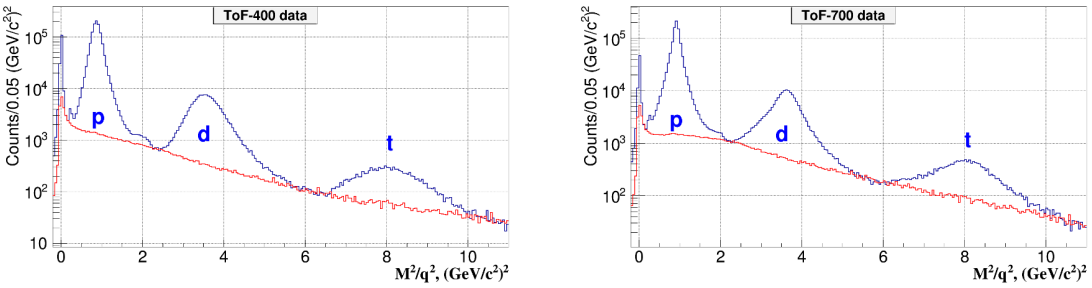


(a) (b)

**Figure 2.** $M^2/q^2$ spectra of positively charged particles produced in argon-nucleus interactions and measured in the ToF-400 (a) and ToF-700 (b) detectors. Peaks of protons, deuterons and tritons with the charge $q = 1$ are indicated; the small peaks of He fragments with $q = 2$ either overlap with the deuteron peaks ($^4$He) or show up at $M^2/q^2 \sim 2\,(\mathrm{GeV/c^2})^2$ ($^3$He). The background estimated from "mixed events" is shown by the red line histograms.

- Momentum range of positively charged particles is limited by the acceptance of the ToF-400 and ToF-700 detectors to $p > 0.5\,\mathrm{GeV/c}$ and $p > 0.7\,\mathrm{GeV/c}$, respectively.

- Distance of extrapolated tracks to the CSC (DCH) hits as well as to the ToF-400 (ToF-700) hits should be within $\pm 2.5\sigma$ of the momentum dependent hit-track residual distributions.

The mass squared ($M^2$) spectra of positively charged particles produced in interactions of the 3.2 A GeV argon beam with various targets are shown in figures 2(a) and 2(b) for ToF-400 and ToF-700 data, respectively. Particles that satisfy the above selection criteria contribute to the $M^2$ spectra. The proton, deuteron and triton signals are extracted in $M^2$ windows, which depend on rapidity, and extend within 0.4–1.7 $(\mathrm{GeV/c^2})^2$, 2.3–5.0 $(\mathrm{GeV/c^2})^2$ and 6.6–10.0 $(\mathrm{GeV/c^2})^2$, at the maximal rapidity, respectively. The signals of protons, deuterons and tritons and their statistical errors are calculated as: $sig = hist - bg$, where $hist$ denotes the histogram integral yield within the selected $M^2$-window, and $bg$ is the background.

The shape of the background under the proton, deuteron and triton signals in the $M^2$ spectra is estimated using the "mixed event" method. For that, tracks reconstructed in the central tracker are matched to hits in the ToF detectors taken from different events containing a similar number of tracks. The "mixed event" background is normalized to the integral of the signal histogram outside the $M^2$ windows of protons, deuterons and tritons. It is found that the background level differs for light and heavy targets and for different intervals of rapidity and transverse momentum.

The ToF-400 and ToF-700 detectors cover different ranges of rapidity and transverse momentum of detected particles. The deuteron signals from Ar+Sn interactions measured by ToF-400 and ToF-700 are shown in figure 3 in the rapidity vs. transverse momentum plane before making any efficiency corrections.

The $dE/dx$ information from the GEM detectors is used to separate the deuteron signals from the overlapping TOF $^4$He signals. The fraction of $^4$He in the entire $^4$He+$d$ sample is determined in rapidity and transverse momentum bins and subtracted from the deuteron TOF



JHEP08(2025)095

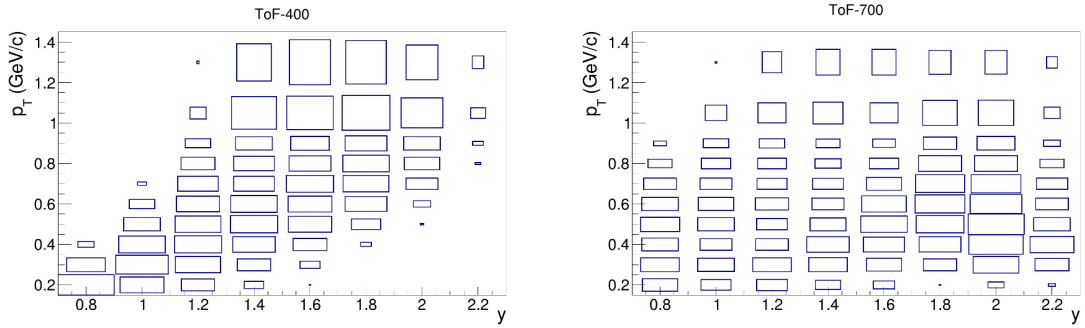


(a) (b)

**Figure 3.** Distribution of the deuteron signals measured in ToF-400 (a) and ToF-700 (b) in the rapidity vs. transverse momentum plane in Ar+Sn interactions.

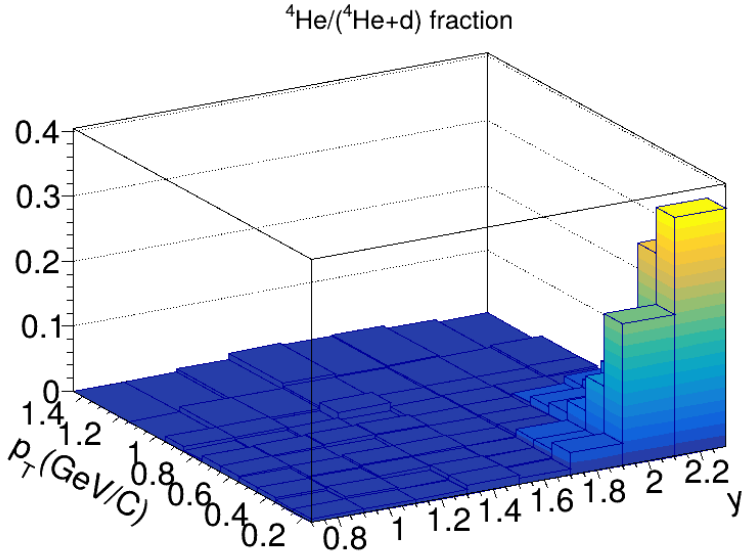


**Figure 4.** Fraction of $^4$He in the $^4$He+$d$ sample measured in the rapidity vs. transverse momentum plane in Ar+A interactions.

signals. The $^4$He fraction combined for all the targets is presented in figure 4. As can be seen, in most of the $y - p_T$ bins, the $^4$He fraction is below 3%. However, it reaches 20–35% in a few bins at large $y$ and low $p_T$, associated with spectator $d$ and $^4$He, with a large fraction of $^4$He.

## 4 Reconstruction efficiency and trigger performance

In order to evaluate the proton, deuteron and triton reconstruction efficiency, Monte Carlo data samples of argon-nucleus collisions were produced with the DCM-SMM [23, 24] event generator. The propagation of particles through the entire detector volume and responses of the detectors were simulated using the GEANT3 toolkit [35] integrated into the BmnRoot software framework [36].

The Monte Carlo events passed through the same chain of reconstruction and identification as the experimental ones. The efficiencies of the silicon, GEM, CSC, DCH and ToF detectors



JHEP08(2025)095

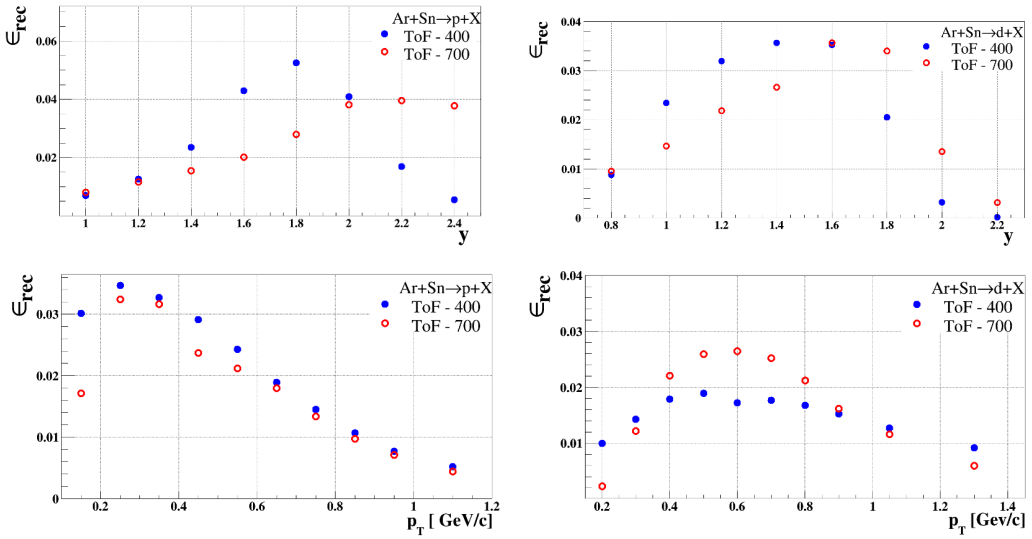


**Figure 5.** Reconstruction efficiency of protons (a) and deuterons (b) produced in Ar+Sn collisions, detected in ToF-400 (full blue circles) and ToF-700 (open red circles) as functions of rapidity $y$ and $p_T$, see text for details.

were adjusted in the simulation in accordance with the measured detector efficiencies [37]. More details of the simulation are given in ref. [8].

The proton, deuteron and triton reconstruction efficiencies are calculated in intervals of rapidity $y$ and transverse momentum $p_T$. The reconstruction efficiency includes geometrical acceptance, detector efficiency, kinematic and spatial cuts, and the loss of protons, deuterons and tritons due to in-flight interactions. The resulting reconstruction efficiencies in ToF-400 and ToF-700 are shown in figure 5 for protons (left) and deuterons (right) from Ar+Sn interactions as functions of $y$ (upper panels) and $p_T$ (lower panels).

The trigger efficiency $\epsilon_{\text{trig}}$ depends on the number of fired channels in the BD (SiMD) detectors. It was calculated for events with reconstructed protons, deuterons and tritons using event samples recorded with an independent trigger based on the SiMD (BD) detectors. The BD and SiMD detectors cover different and non-overlapping regions of the BM@N acceptance, that is, they detect different collision products.

The efficiency of the combined BD and SiMD triggers was calculated as the product of the efficiencies of the BD and SiMD triggers. The trigger efficiency decreases with the decrease of the target mass and with the increase of the collision centrality. More details on the evaluation of the trigger efficiencies are given in ref. [8]. In particular, as illustrated in figure 10 of [8], the trigger system accepts events in the full centrality range.

## 5 Centrality classes

The nucleus-nucleus collision centrality is defined as the ratio of the interaction cross section corresponding to a given impact parameter interval $[0, b]$ to the total inelastic interaction cross section. Two classes of centrality: 0–40% (more central collisions) and 40–80% (more



JHEP08(2025)095

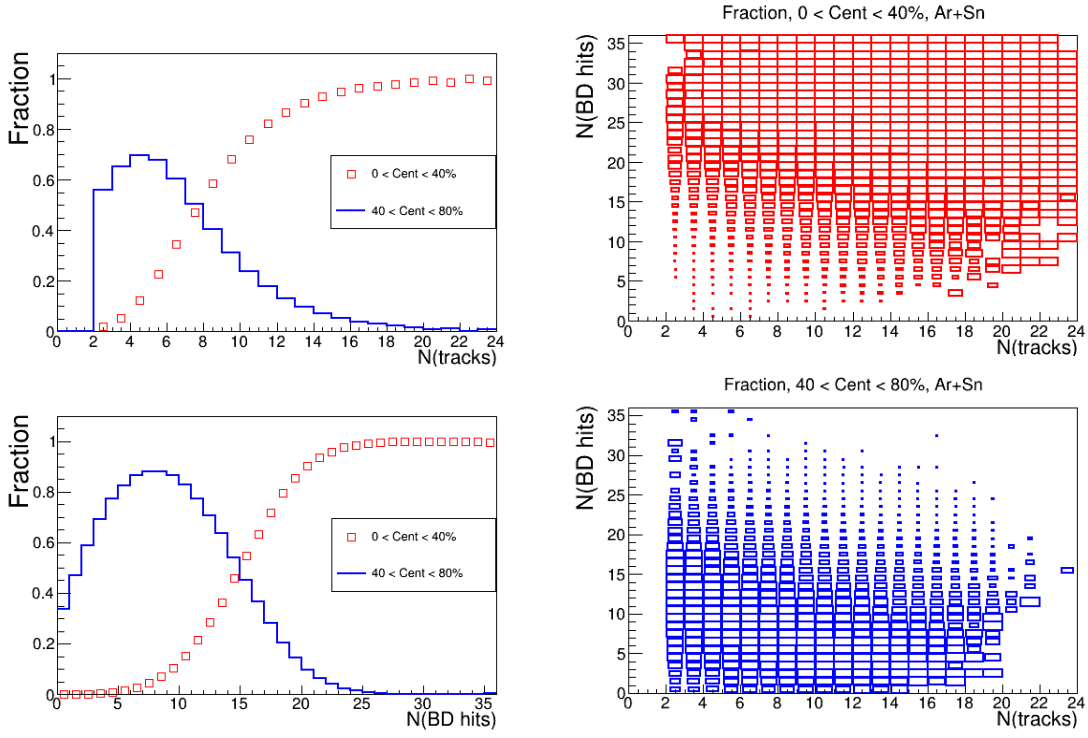


**Figure 6.** (a) Probability distribution of the number of tracks N(tracks) in the primary vertex (upper panel) and the number of hits N(BD) in the BD detector (lower panel) for events with centrality 0–40% (red open symbols) and 40–80% (blue histogram); (b) two-dimensional plot of the probability distribution of N(tracks) (horizontal axis) vs. N(BD) (vertical axis) in events with centrality 0–40% (upper panel) and 40–80% (lower panel).

| | Ar+C | Ar+Al | Ar+Cu | Ar+Sn | Ar+Pb |
|---|---|---|---|---|---|
| $b_{40}$, fm | 4.23 | 4.86 | 5.66 | 6.32 | 7.10 |
| $b_{80}$, fm | 6.2 | 7.0 | 8.0 | 9.0 | 10.0 |
| $\sigma_{\text{inel}}$, mb [38] | $1470 \pm 50$ | $1860 \pm 50$ | $2480 \pm 50$ | $3140 \pm 50$ | $3940 \pm 50$ |

**Table 1.** Boundary impact parameters $b_{40}$ and $b_{80}$ for the definition of the centrality classes 0–40% and 40–80% and the inclusive inelastic cross section $\sigma_{\text{inel}}$ [38] for Ar+A interactions.

peripheral collisions) are defined from the impact parameter distributions of Ar+A inelastic interactions simulated by the DCM-SMM model. The boundary impact parameters $b_{40}$ and $b_{80}$ for the definition of the two classes for interactions of Ar with various targets are given in table 1. It was found that the number of tracks originating from the primary event vertex N(tracks) and the number of hits in the Barrel Detector N(BD) are anti-correlated with the impact parameter $b$. Using the results of the DCM-SMM Monte Carlo simulation, the fractions of reconstructed events, which belong to the centrality classes 0–40% and 40–80%, are calculated. Fractions of events with centrality 0–40% and 40–80% are presented in figure 6 as functions of N(tracks), N(BD) and as a two-dimensional distribution N(tracks)/N(BD).



JHEP08(2025)095

Fractions (probabilities) of events with centrality 0–40% and 40–80%, taken from the two-dimensional N(tracks)/N(BD) distributions, are used as event weights to define the weighted numbers of reconstructed protons, deuterons and tritons in the $y$ and $p_T$ bins in data as well as in simulation. The systematic uncertainty of the event centrality is estimated from the remaining difference between the simulations and data in the shape of the N(tracks) and N(BD) distributions in $y$ and $p_T$ bins.

## 6 Cross sections, multiplicities and systematic uncertainties

The protons, deuterons and tritons from interactions of Ar with C, Al, Cu, Sn and Pb are measured in the following kinematic ranges: transverse momentum $0.1 < p_T < 1.2\,\mathrm{GeV/c}$ (protons), $0.15 < p_T < 1.45\,\mathrm{GeV/c}$ (deuterons), $0.2 < p_T < 1.6\,\mathrm{GeV/c}$ (tritons) and rapidity in the laboratory frame $0.9 < y < 2.5$ (protons), $0.7 < y < 2.3$ (deuterons), $0.7 < y < 2.1$ (tritons). The differential cross sections $d^2\sigma_{p,d,t}(y,p_T)/dydp_T$ and multiplicities $d^2N_{p,d,t}(y,p_T)/dydp_T$ of protons, deuterons and tritons produced in Ar+C, Al, Cu, Sn and Pb interactions are calculated using the relations:

$$\begin{aligned} d^2\sigma_{p,d,t}(y,p_T)/dydp_T &= \Sigma[d^2n_{p,d,t}(y,p_T,N_{\mathrm{tr}})/(\epsilon_{\mathrm{trig}}(N_{\mathrm{tr}})dydp_T)] \times 1/(L\epsilon^{\mathrm{rec}}_{p,d,t}(y,p_T)) \\ d^2N_{p,d,t}(y,p_T)/dydp_T &= d^2\sigma_{p,d,t}(y,p_T)/(\sigma_{\mathrm{inel}}dydp_T), \end{aligned} \tag{6.1}$$

where the sum is performed over bins of the number of tracks in the primary vertex $N_{\mathrm{tr}}$; $n_{p,d,t}(y,p_T,N_{\mathrm{tr}})$ is the number of reconstructed protons, deuterons and tritons in the intervals $dy$ and $dp_T$; $\epsilon_{\mathrm{trig}}(N_{\mathrm{tr}})$ is the track-dependent trigger efficiency; $\epsilon^{\mathrm{rec}}_{p,d,t}(y,p_T)$ is the reconstruction efficiency of protons, deuterons and tritons; $L$ is the luminosity; and $\sigma_{\mathrm{inel}}$ is the inelastic cross section for argon-nucleus interactions. The cross sections and multiplicities are evaluated for the two centrality classes: 0–40% and 40–80%.

Several sources of systematic uncertainties are considered in evaluating the uncertainties of the measured proton, deuteron and triton yields $n_{p,d,t}$ and the reconstruction efficiency $\epsilon_{\mathrm{rec}}$. Some of them affect both the yield $n_{p,d,t}$ and the reconstruction efficiency $\epsilon_{\mathrm{rec}}$. For these cases, the impact of correlations between them on the $n_{p,d,t}/\epsilon_{\mathrm{rec}}$ ratio is taken into account. The systematic uncertainties associated with the track reconstruction as well as with the trigger efficiency are discussed in detail in ref. [8]. Additional sources specific to this analysis are listed below:

- Systematic uncertainty of the background subtraction in the mass-squared $M^2$ spectra of identified particles: it is estimated as the difference between the background integral under the $p$, $d$, $t$ mass-squared windows taken from "mixed events" (as described in section 3) and from the fitting of the $M^2$ spectra by a linear function. The latter is done in the $M^2$ range, excluding the proton, deuteron and triton signal windows.

- Systematic uncertainty calculated as half of the difference between the $p/d/t$ yield measured in the ToF-400 and ToF-700 detectors in bins of rapidity $y$.

- Systematic uncertainty of the event centrality weights estimated (i) from the remaining difference in the shape of the N(track) and N(BD) distributions in $y$ and $p_T$ bins in the



JHEP08(2025)095

| | Ar+C | Ar+Al | Ar+Cu | Ar+Sn | Ar+Pb |
|---|---|---|---|---|---|
| $\epsilon_{\text{trig}}$ $p, d, t$ | 9 | 7 | 7 | 7 | 7 |
| protons | | | | | |
| $n_p/\epsilon_{\text{rec}}$ | 15 | 6 | 8 | 14 | 11 |
| Total | 18 | 9 | 11 | 16 | 13 |
| deuterons | | | | | |
| $n_d/\epsilon_{\text{rec}}$ | 32 | 22 | 20 | 19 | 22 |
| Total | 33 | 23 | 21 | 20 | 23 |
| tritons | | | | | |
| $n_t/\epsilon_{\text{rec}}$ | 43 | 22 | 20 | 20 | 22 |
| Total | 44 | 23 | 21 | 21 | 23 |

**Table 2.** Mean relative systematic uncertainties (in %) averaged over the $y$, $p_T$ ranges of protons, deuterons and tritons measured in argon-nucleus interactions.

data and the simulation; (ii) from the difference in the event centrality weights taken from the two-dimensional N(track)/N(BD) distribution relative to the one-dimensional N(BD) distribution.

Table 2 summarizes the mean values (averaged over $p_T$, $y$ and $N_{\text{tr}}$) of the systematic uncertainties of the various factors of eq. (6.1), $n_{p,d,t}$, $\epsilon_{\text{rec}}$, and $\epsilon_{\text{trig}}$. The total systematic uncertainty from these sources, calculated as the square sum of their uncertainties from different sources, is listed in table 2 for each target.

The luminosity is calculated from the beam flux $\Phi$ as given by the beam trigger (see section 2) and the target thickness $l$ using the relation $L = \Phi\rho l$, where $\rho$ is the target density expressed in atoms/cm$^3$. The systematic uncertainty of the luminosity is estimated from the fraction of the beam that can miss the target, determined from the vertex positions, and found to be within 2%. The inelastic cross sections of Ar+C, Al, Cu, Sn and Pb interactions are taken from the predictions of the DCM-SMM model. The $\sigma_{\text{inel}}$ uncertainties for Ar+C, Al, Cu, Sn and Pb interactions given in table 1 are estimated from the empirical formulae taken from refs. [38, 39].

## 7 Rapidity and transverse mass spectra

At a kinetic energy of 3.2 A GeV, the rapidity of the nucleon-nucleon center-of-mass (CM) system is $y_{\text{CM}} = 1.08$. The rapidity intervals covered in the present measurements, $0.9 < y < 2.5$, $0.7 < y < 2.3$ and $0.7 < y < 2.1$ for protons, deuterons and tritons, respectively, correspond, therefore, to the forward and central rapidity regions in the nucleon-nucleon CM system. The measured yields of protons, deuterons and tritons in $m_T$ and $y$ bins in the two centrality intervals in Ar+C, Al, Cu, Sn and Pb interactions can be found in ref. [40].

As an example, figure 7 shows the invariant transverse mass $m_T = \sqrt{m^2 + p_T^2}$ spectra of protons, deuterons and tritons ($m = m_{p,d,t}$) produced at $y = 1.4$ in Ar+A collisions in the 0–40% centrality class. The spectra are parameterized by an exponential function as:

$$\frac{1}{m_T} d^2N/dydm_T = \frac{dN/dy}{T_0(T_0 + m)} \exp(-(m_T - m)/T_0), \tag{7.1}$$



JHEP08(2025)095

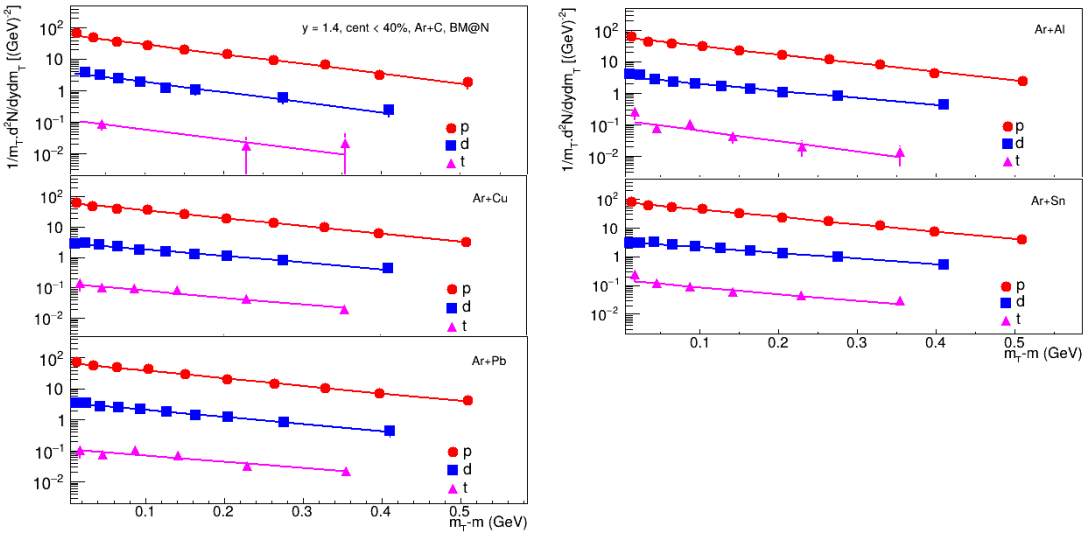


**Figure 7.** Invariant transverse mass spectra of protons, deuterons and tritons produced at rapidity $y = 1.4$ in Ar+C, Al, Cu, Sn and Pb interactions with centrality 0–40%. The vertical bars and boxes represent the statistical and systematic uncertainties, respectively. The lines show the results of the fit by an exponential function.

where the fitting parameters are the integral of the $m_T$ spectrum, $dN/dy$, and the inverse slope, $T_0$. The $dN/dy$ and $T_0$ values extracted from the fit can be found in ref. [40].

The $dN/dy$ distributions of protons, deuterons and tritons produced in Ar+A collisions with centrality 0–40% are shown in figures 8(a), 9(a) and 10(a). The comparison of the measurements with the predictions of the DCM-SMM and PHQMD models is also shown in these figures. The boundary impact parameters $b_{40}$ and $b_{80}$ listed in table 1 are used to define the centrality classes in the model calculations.

As can be seen, the shapes of the rapidity distributions of $p$, $d$, $t$ essentially vary with the target mass. For protons, the predictions of two models are quite similar and they are in reasonable agreement with the experimental results in the forward rapidity range except for Ar+C interactions, where the models underestimate the data.

Deuterons and tritons are produced mostly in the beam fragmentation region for Ar+C and Ar+Al interactions, whereas they are mostly produced at mid-rapidity on heavier targets. For deuterons, the DCM-SMM and PHQMD models reasonably describe the shape of the experimental spectra but underestimate the absolute yields by factors of about 3 and 2, respectively. The triton yields predicted by the models are below the experimental data by a factor of about 5.

The $dN/dy$ distributions of protons, deuterons and tritons produced in Ar+A collisions with centrality 40–80% are shown in figures 8(b), 9(b) and 10(b). The largest contribution is observed in the beam fragmentation region for all the targets. This tendency is described by the DCM-SMM and PHQMD models. Again, the models underestimate the absolute yields for deuterons by factors of 3 and 2, respectively. The triton yields predicted by the models are below the experimental data by a factor of about 5. A significant deficit of deuterons and tritons in the PHQMD model relative to the experimental data has also been observed in central (0–10%) Au+Au collisions at $\sqrt{s_{\rm NN}} = 3\,$GeV by the STAR experiment [41].



JHEP08(2025)095

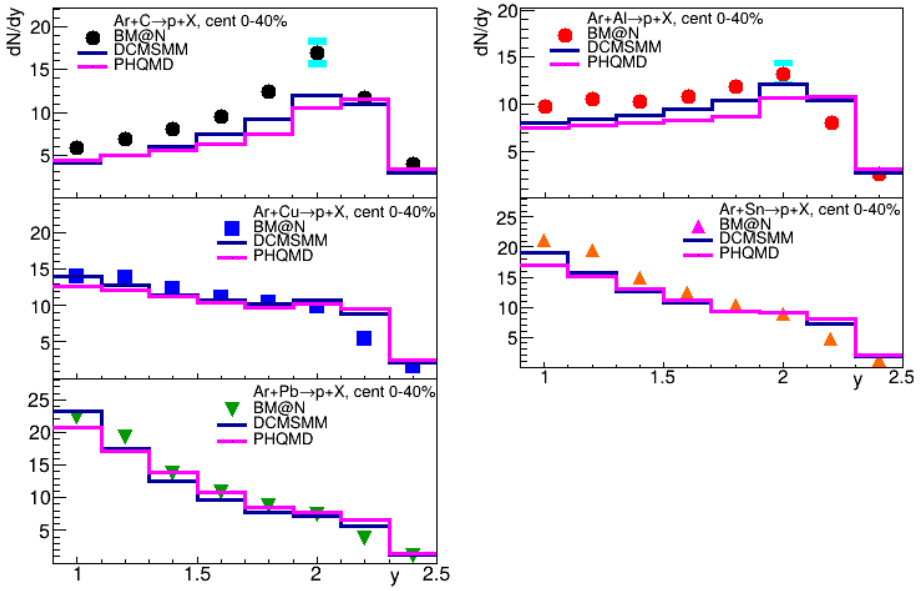


(a)

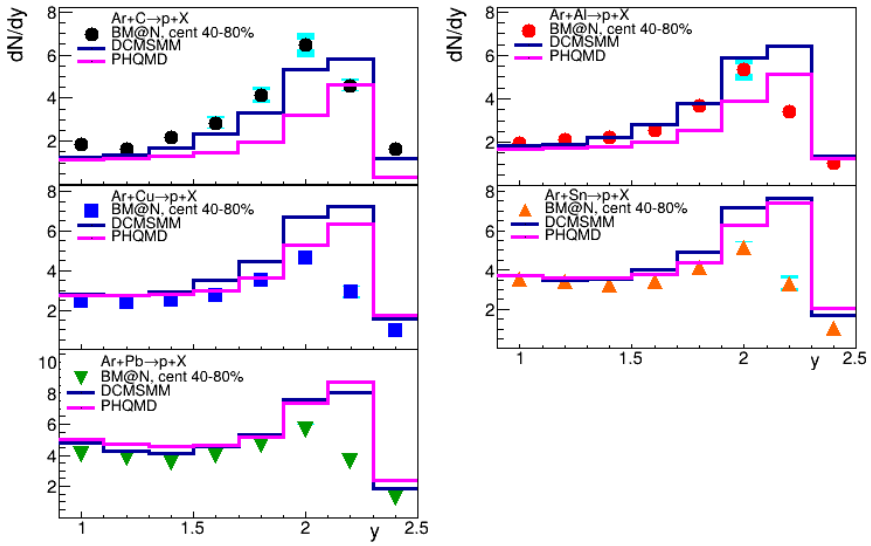


(b)

**Figure 8.** Rapidity distributions $dN/dy$ of protons produced in Ar+C, Al, Cu, Sn and Pb interactions at 3.2 A GeV with centrality 0–40% (a) and 40–80% (b). The results are integrated over $p_T$. The vertical bars and boxes represent the statistical and systematic uncertainties, respectively. The predictions of the DCM-SMM and PHQMD models are shown as blue and magenta histograms.

JHEP08(2025)095

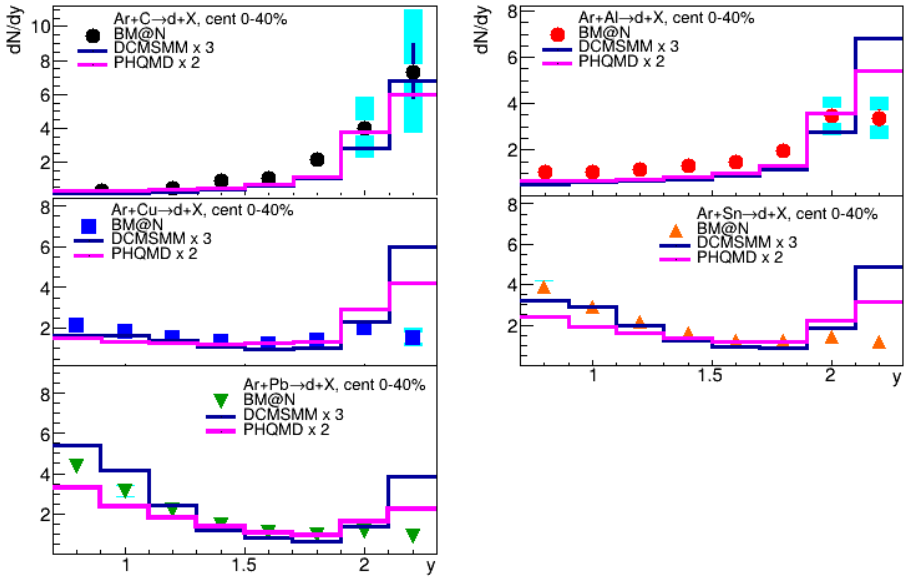


(a)

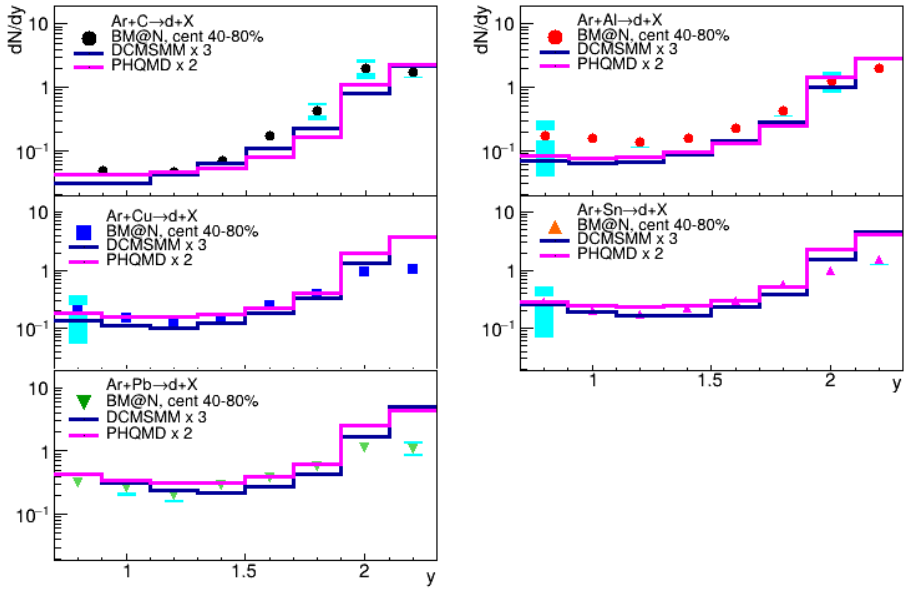


(b)

**Figure 9.** Rapidity distributions $dN/dy$ of deuterons produced in Ar+C, Al, Cu, Sn and Pb interactions with centrality 0–40% (a) and 40–80% (b). The results are integrated over $p_T$. The vertical bars and boxes represent the statistical and systematic uncertainties, respectively. The predictions of the DCM-SMM and PHQMD models, multiplied by factors of 3 and 2, respectively, are shown as blue and magenta histograms.

JHEP08(2025)095

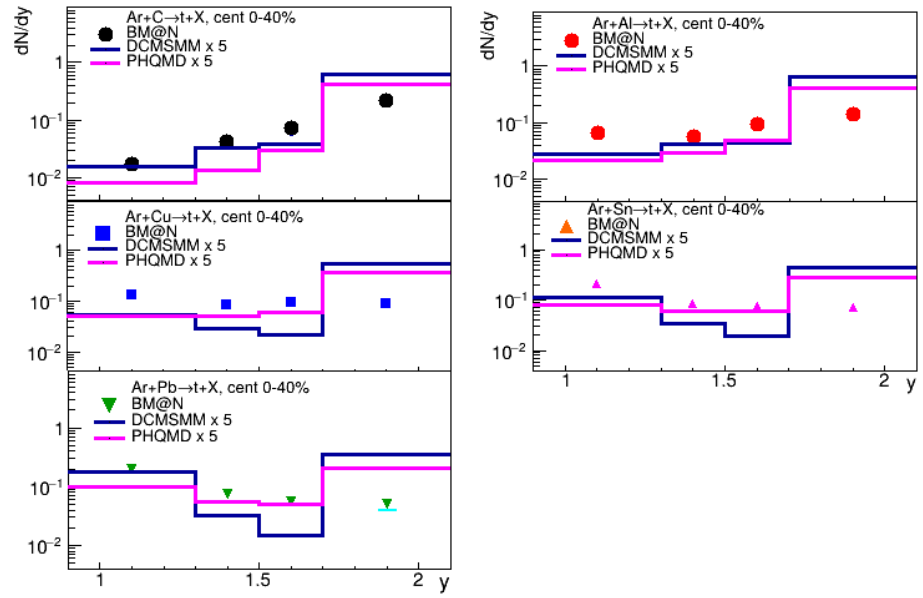


(a)

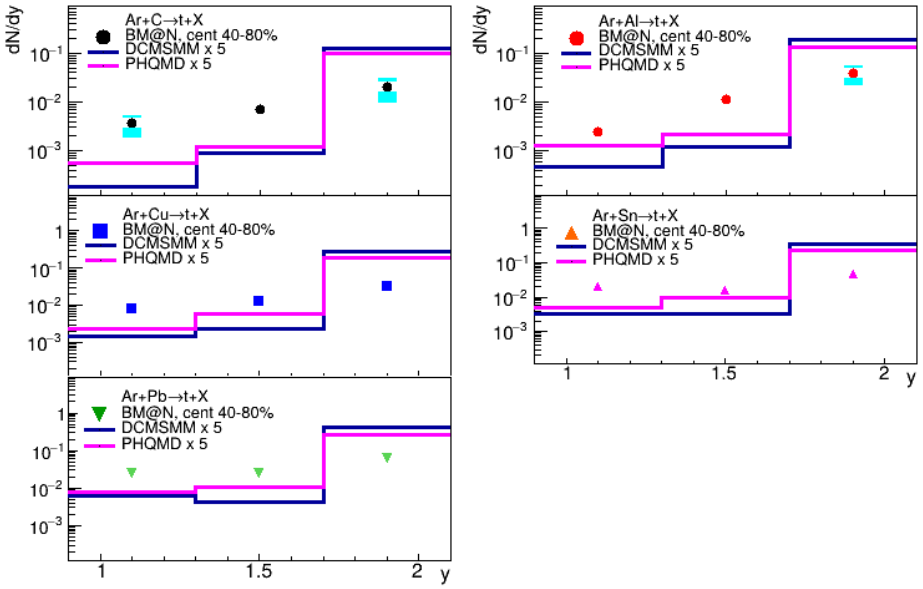


(b)

**Figure 10.** Rapidity distributions $dN/dy$ of tritons produced in Ar+C, Al, Cu, Sn and Pb interactions with centrality 0–40% (a) and 40–80% (b). The results are integrated over $p_T$. The vertical bars and boxes represent the statistical and systematic uncertainties, respectively. The predictions of the DCM-SMM and PQHMD models, multiplied by a factor of 5, are shown as blue and magenta histograms.

JHEP08(2025)095

The observed discrepancy between the data and the DCM-SMM and PHQMD models could be partially explained by feed-down from excited nuclear states, which are not taken into account in the models. At BM@N collision energies, the reaction zone consists of a hadronic gas dominated by nucleons and stable nuclei, in particular, $d$, $t$, $^3$He, $^4$He. However, in addition to these nuclei, there are many excited nuclear states with the mass number $A \geqq 4$. The role of the feed-down from these states for the description of light nuclei production in a broad energy range was discussed in ref. [42]. As reported in [42], feeding gives a significant contribution to the yields of $d$, $t$ at NICA/BM@N energies: as much as 60% of all final tritons and 20% of deuterons may come from the decays of excited nuclear states.

The mean transverse kinetic energy, defined as $\langle E_T \rangle = \langle m_T \rangle - m$, is related to the $T_0$ value extracted from the fit of the $m_T$ spectrum by the following equation:

$$\langle E_T \rangle = \langle m_T \rangle - m = T_0 + T_0^2/(T_0 + m). \tag{7.2}$$

The $\langle E_T \rangle$ values of protons in the 0–40% centrality class are shown in figure 11(a) as a function of rapidity. The maximal values of $\langle E_T \rangle$ are measured at rapidity $1.0 < y < 1.3$, i.e., at mid-rapidity in the CM system. In general, the $y$-dependence of $\langle E_T \rangle$ for protons is consistent with the predictions of the DCM-SMM and PHQMD models.

The $\langle E_T \rangle$ values for deuterons and tritons in the 0–40% centrality class are shown as functions of rapidity in figures 11(b) and 11(c), respectively. PHQMD reproduces the rise of the data at mid-rapidity in CM for deuterons and tritons relative to protons, whereas the DCM-SMM model predicts similar $\langle E_T \rangle$ values f or protons, deuterons and tritons contrary to the experimental results.

A Blast-Wave model [50] was used to fit the invariant transverse mass spectra of protons, deuterons and tritons according to a formula valid on the assumption of a box-like density profile with a uniform density inside the fireball (thermal source) region of transverse radius $r \leq R$:

$$\frac{d^2N}{m_T dm_T dy} = \mathrm{Norm}(y) \int_0^R m_T K_1 \left( \frac{m_T \cosh \rho(r)}{T} \right) I_0 \left( \frac{p_T \sinh \rho(r)}{T} \right) r dr, \tag{7.3}$$

where $\mathrm{Norm}(y)$ is the normalization factor, $I_0$ and $K_1$ are the modified Bessel functions, $T$ is the kinetic freeze-out temperature and $\rho(r) = \tanh^{-1} \beta(r)$ is the transverse radial flow rapidity profile. The transverse radial flow velocity $\beta(r)$ inside the fireball region is usually parametrized as $\beta = \beta_s (r/R)^n$, where $\beta_s$ is the fireball-surface velocity. Assuming a linear velocity profile (exponent $n = 1$), one gets an average transverse radial flow velocity $\langle \beta \rangle = (2/3)\beta_s$. The invariant $m_T$-spectra of $p$, $d$, $t$ produced at $y = 1.4$ in Ar+C, Al, Cu, Sn and Pb interactions with centrality 0–40% are shown in figure 12. The average radial flow velocity $\langle \beta \rangle$ and source temperature $T$ at the kinetic freeze-out extracted from the Blast-Wave model fits to the transverse mass spectra of protons, deuterons and tritons measured in the range $0.9 < y < 1.5$ ($-0.18 < y^* < 0.42$ in the center-of-mass system) are given in table 3. The quadratic sum of the statistical and systematical uncertainties of data points are used to evaluate the errors of the fit parameters. The parameters of the fit were assumed to be constant in the rapidity range of the fit. If a functional form of the Boltzmann approximation $T(0)/\cosh y^*$ with the midrapidity temperature $T(0)$ is used instead, the difference in the fit result is within 5%.



JHEP08(2025)095

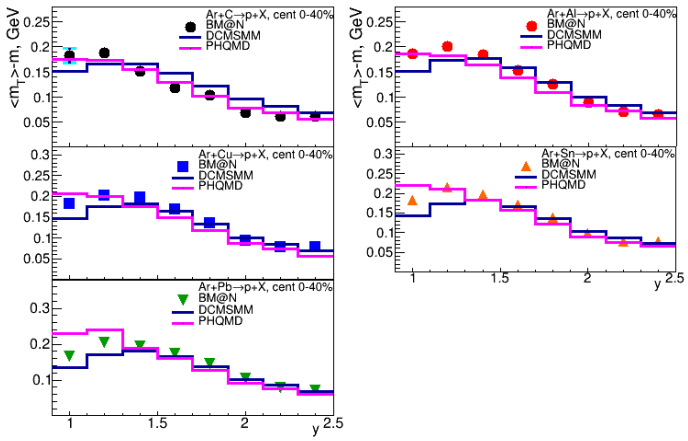


(a)

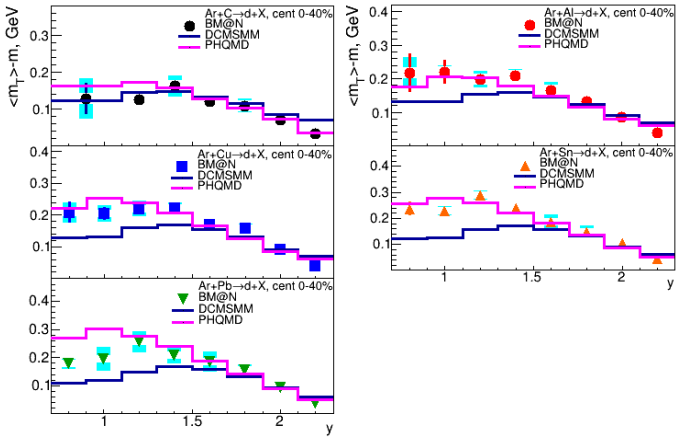


(b)

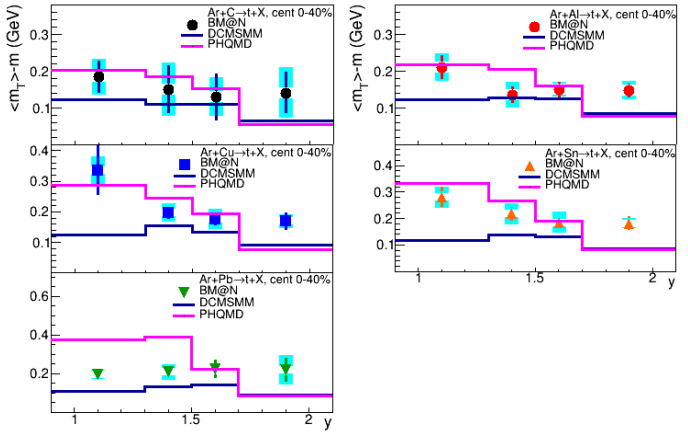


(c)

**Figure 11.** Mean transverse kinetic energy $\langle E_T \rangle = \langle m_T \rangle - m$ of protons (a), deuterons (b) and tritons (c) in Ar+C, Al, Cu, Sn and Pb interactions with centrality 0–40% as functions of rapidity $y$. The vertical bars and boxes represent the statistical and systematic uncertainties, respectively. The predictions of the DCM-SMM and PHQMD models are shown as blue and magenta histograms.



JHEP08(2025)095

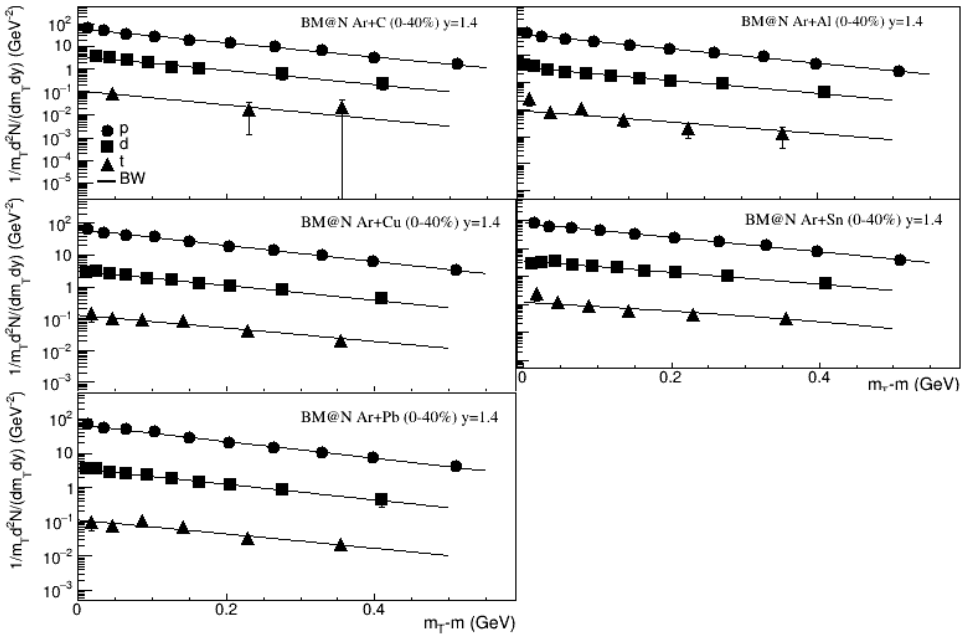


**Figure 12.** Invariant $m_T$-spectra of $p$, $d$, $t$ produced at rapidity $y = 1.4$ in 0–40% central Ar+A interactions. The BM@N data are shown by various symbols, the fits motivated by the Blast-Wave model are drawn by lines.

| | Ar+C | Ar+Al | Ar+Cu | Ar+Sn | Ar+Pb |
|---|---|---|---|---|---|
| T, MeV | $140 \pm 18$ | $129 \pm 10$ | $132 \pm 11$ | $113 \pm 10$ | $126 \pm 12$ |
| $\langle\beta\rangle$ | $0.0\pm^{0.12}_{0.0}$ | $0.19 \pm 0.05$ | $0.21 \pm 0.04$ | $0.27 \pm 0.03$ | $0.23 \pm 0.05$ |
| $\chi^2/ndf$ | 44/49 | 127/55 | 113/55 | 86/55 | 172/55 |

**Table 3.** $T$ and $\langle\beta\rangle$ values evaluated from the Blast-Wave fit of the transverse mass spectra of protons, deuterons and tritons produced in the CM system rapidity range $-0.18 < y^* < 0.42$ in Ar+A interactions with centrality 0–40%. The errors represent the uncertainties of the fit to the data points with the quadratic sum of the statistical and systematical uncertainties.

One may also obtain the temperature $T$ and mean transverse radial flow velocity $\langle\beta\rangle = 2/(n+2)\beta_s$ from common fits of transverse kinetic energies $\langle E_T\rangle$ of protons, deuterons and tritons using the formula derived from eq. (7.3) in the limit of small $1/z = T/m$ and $\beta_s^2$:

$$\begin{aligned}\langle E_T\rangle = T\Big([1 + 3/(2z) - 9/(8z^2)] + \beta_s^2 z[(1 + 1/z)(1 + 3/z) - 9/(2z^3)]/[2(n + 1)] \\ + \beta_s^4 z[(3 + n(6 + 5n)) + (9 + n(18 + 17n))/z + 3(3 + n(6 + 7n))/(8z^2) \\ - 9(1 + n(2 + 9n))/(8z^3)]/[8(1 + n)^2(1 + 2n)]\Big),\end{aligned} \tag{7.4}$$

valid up to terms $O(1/z^3)$ and $O(\beta_s^6)$. Note that at temperatures $T$ of a hundred MeV, the $\beta_s^2$-term in eq. (7.4) is nearly linear in the cluster mass $m$ down to the proton mass. The fitted parameters agree with those in table 3, except for approximately 50% larger errors due to the integration in $\langle E_T\rangle$ of part of the information contained in the $m_T$ spectra.



JHEP08(2025)095

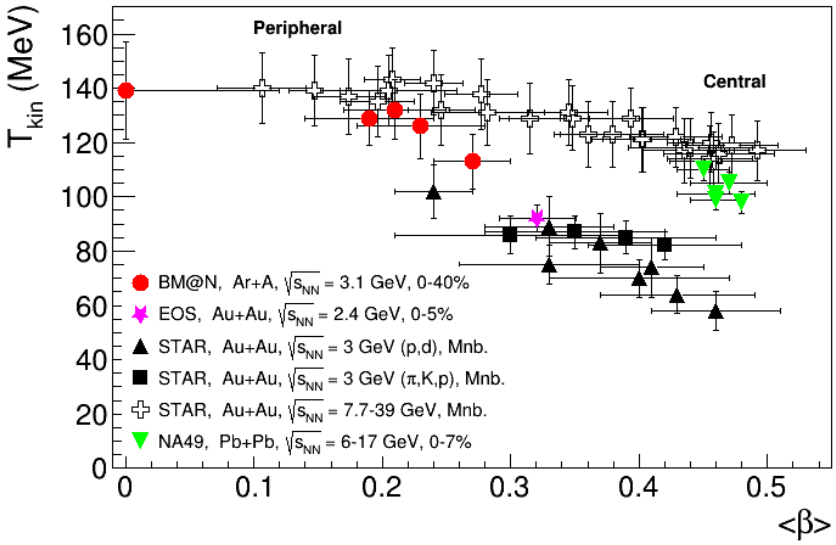


**Figure 13.** Kinetic freeze-out parameters ($T_{\rm kin}$ and $\langle\beta\rangle$) in centrality selected nucleus-nucleus collisions: Ar+A (this study); Au+Au from EOS [46] and STAR [47–49]; Pb+Pb from NA49 [44]. For the STAR results, "Mnb." stands for minimum bias, the labels "Peripheral" and "Central" indicate the most peripheral (70–80% central) and the most central (0–5% central) bins of Au+Au collisions, respectively.

One finds a flow velocity consistent with zero in central Ar+C collisions. Nuclear collisions of such small systems can be considered as a superposition of independent nucleon-nucleon interactions; therefore, the density of participants reached in these reactions is probably not high enough to create a fireball with a strong collective behavior. In contrast, for larger colliding systems (Ar+Al, Cu, Sn and Pb), the particle density and re-scattering rate inside the reaction zone are higher, giving rise to a collective flow velocity. It appears that the observed target mass dependence for $T$ and $\langle\beta\rangle$ is weak at BM@N energies: fitted temperature and mean flow velocity are practically the same within the errors for studied colliding systems. This might be an indication that the increase of the reaction volume and the number of collisions with the target mass is not accompanied by a significant compression of the nuclear matter.

The BM@N results for kinetic freeze-out parameters ($T_{\rm kin}$ and $\langle\beta\rangle$) could be compared with measurements at lower and higher energies. Figure 13 presents results for centrality-selected nucleus-nucleus collisions from the BM@N experiment (this study, 0–40% central Ar+A at $\sqrt{s_{\rm NN}} = 3.1\,$GeV), the EOS experiment [46] (0–5% central Au+Au at $\sqrt{s_{\rm NN}} = 2.4\,$GeV), the STAR experiment [47, 48] (0–5%, 5–10%, 10–20%, . . . , 70–80% central Au+Au at $\sqrt{s_{\rm NN}} = 7.7$–$39\,$GeV), and the NA49 experiment [44] (0–7% central Pb+Pb at $\sqrt{s_{\rm NN}} = 6.2$–$17.3\,$GeV). Preliminary STAR results from a Blast-Wave analysis of hadron and light nuclei spectra in centrality-selected Au+Au collisions at $\sqrt{s_{\rm NN}} = 3\,$GeV [49] are also presented. These results are shown for different combinations of particle species used in the Blast-Wave fits: light hadrons $(\pi, K, p)$ or protons and deuterons $(p, d)$. Though the quoted uncertainties in a Blast-Wave motivated analysis are large, there is an indication that the system size trend for kinetic freeze-out parameters is different in low ($\sqrt{s_{\rm NN}} < 6\,$GeV) and high-energy collisions.



JHEP08(2025)095

## 8 Coalescence factors

Within a coalescence model [18, 19, 21], nuclear fragment formation is characterized by a coalescence factor $B_A$, defined through the invariant momentum spectra by the equation:

$$E_A d^3N_A/d^3p_A = B_A(E_p d^3N_p/d^3p)^Z (E_n d^3N_n/d^3p)^{A-Z}_{|p=p_A/A},$$

where $p_A$ and $p = p_A/A$ are momenta of the nuclear fragment A and the nucleon, respectively. It relates the yield $N_A$ of nuclear fragments with charge $Z$ and atomic mass number $A$ to the yields of the coalescing nucleons $N_p$ and $N_n$ at the same velocity. Assuming that neutron momentum density is equal to the proton momentum density at freeze-out, the $B_A$ value can be calculated as:

$$B_A = d^2N_A/2\pi p_{T,A} dp_{T,A} dy/(d^2N_p/2\pi p_T dp_T dy)^A/(n/p)^{A-Z}, \tag{8.1}$$

where $n/p$ is the ratio of the numbers of produced neutrons to protons, $p_{T,A}$ and $p_T$ are the transverse momenta of the nuclear fragment A and the proton, respectively. The coalescence factor is inversely related to the effective emission volume of the nucleons with nearby 3-momenta [21]: $B_A \sim V_{\text{eff}}^{1-A}$. The strong position-momentum correlations present in the expanding source lead to a higher coalescence probability at larger $p_T$ values. Assuming a box-like transverse density profile of the source, the model predicts at small or moderate $p_T$ [22]:

$$B_A \simeq g_s \Lambda_A A^{-1/2} C_A [(2\pi)^{3/2}/(m_T R_\parallel(m_T) R_\perp^2(m_T))]^{A-1} \exp[m_T(1/T_p - 1/T_A)], \tag{8.2}$$

where $g_s = (2S+1)/2^A$ is the spin factor of the nuclear fragment A, $\Lambda_A$ is a suppression factor of correlated nucleons, e.g., due to a feed-down fraction of uncorrelated nucleons produced in hyperon decays, $C_A$ is a quantum correction factor related to the finite fragment size [21, 22], $R_\perp$ and $R_\parallel$ are the femtoscopic radii of the source in the longitudinally co-moving system (LCMS) [22], $T_p$ and $T_A$ are the inverse transverse momentum slopes for proton and fragment A, respectively. The $\Lambda_A$ factor is close to 1 in the BM@N energy range, as the fraction of nucleons originated from hyperon decays is around 2% according to predictions of the UrQMD model [65]. The UrQMD and PHQMD models predict the $n/p$ ratio to be between 1.09 and 1.18 in the BM@N rapidity range for Ar+C and Ar+Pb interactions, respectively (see also section 9).

The $B_2$ and $B_3$ values as functions of the transverse momentum measured in argon-nucleus interactions with centrality 0–40% are shown in figures 14(a) and 14(b), respectively. The transverse momentum is scaled to the atomic number of the nuclear fragment (deuteron, triton), $p_T/A$. The yields of protons ($N_p$), deuterons ($N_d$) and tritons ($N_t$) are measured in the same rapidity range, namely $0.9 < y < 1.7$ ($-0.18 < y^* < 0.62$). The statistics of tritons is not sufficient to present $B_3$ for Ar+C interactions. It is found that $B_2$ and $B_3$ rise with $p_T$ at low $p_T$ and saturate at higher $p_T$ for all the targets used in measurements. The $B_2$ and $B_3$ values at low $p_T$ are smaller for heavier targets compared to lighter targets.

In order to compare the present measurements of $B_2$ and $B_3$ with previously obtained results, the $B_2(p_T)$ and $B_3(p_T)$ values given in figure 14 are extrapolated down to $p_T = 0$ using exponential fits of the form $b\exp[a(m_T - m_A)]$ as predicted by the coalescence model with a box-like density profile [22], see eq. (8.2). The fits are performed for the first four data



JHEP08(2025)095

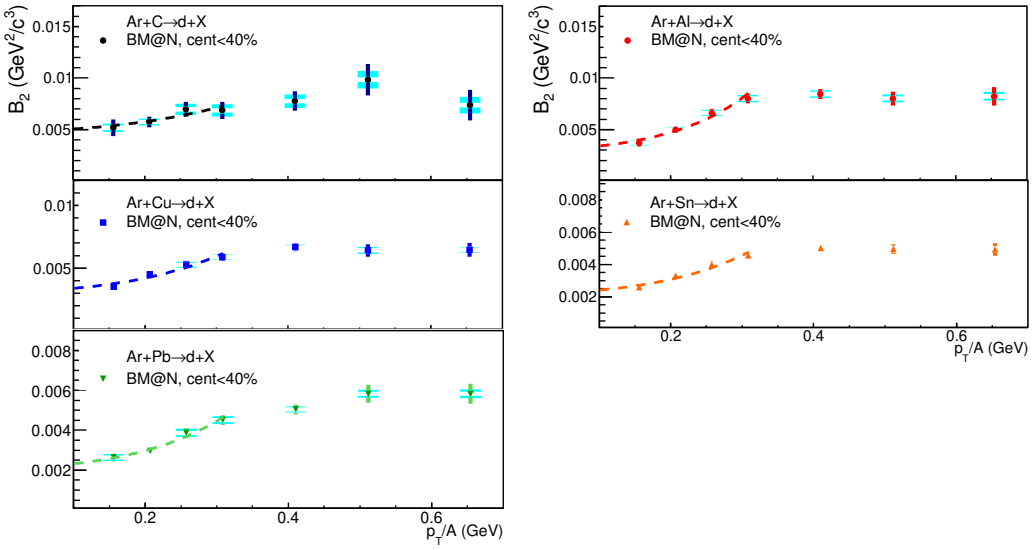


(a)

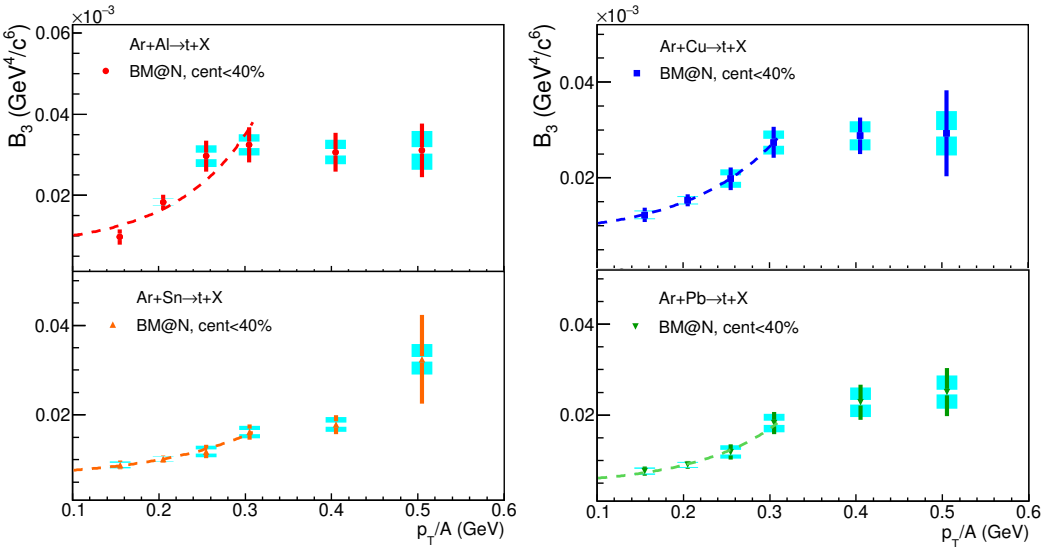


(b)

**Figure 14.** Coalescence parameter $B_2$ for deuterons (a) and $B_3$ for tritons (b) measured as a function of $p_T/A$ in the rapidity range $-0.18 < y^* < 0.62$ in Ar+A collisions with centrality 0–40%. Dash lines show results of the fits in the range $p_T/A < 0.32$ described in the text.

points in the range $p_T/A < 0.32$. If the fit results with $\chi^2/ndf > 1$, the uncertainty of the parameter $B_A(p_T = 0)$ is scaled up by a factor $\sqrt{\chi^2/ndf}$ following a recommendation given in ref. [55, Introduction, section 5.2]. The results of the extrapolation are presented in table 4.

The BM@N values of $B_2 = 1.84 \pm 0.5\,\mathrm{GeV}^2/\mathrm{c}^3$ and $B_3 = 3.5 \pm 1.2\,\mathrm{GeV}^4/\mathrm{c}^6$ calculated as the weighed average values for Ar+Al, Cu, Sn and Pb interactions with centrality 0–40% are compared in figure 15 with the results of other experiments: STAR (0–10% central, $p_T/A = 0.65\,\mathrm{GeV/c}$) [41, 61, 62], NA44 (0–10% central) [56], NA52 [60], E864 [57], E877 [58], E878 [59] (0–10% cental), NA49 (0–7% central) [44]. The $B_2$ and $B_3$ results for Ar+A



JHEP08(2025)095

| | Ar+C | Ar+Al | Ar+Cu | Ar+Sn | Ar+Pb |
|---|---|---|---|---|---|
| $-0.18 < y^* < 0.22$ | | | | | |
| $B_2(p_T = 0)/10^3$, GeV$^2$/c$^3$ | $3.2 \pm 1.0$ | $1.95 \pm 0.7$ | $2.6 \pm 0.3$ | $1.8 \pm 0.2$ | $1.35 \pm 0.2$ |
| $B_3(p_T = 0)/10^6$, GeV$^4$/c$^6$ | — | $7.2 \pm 2.2$ | $5.8 \pm 2.8$ | $4.9 \pm 0.6$ | $2.6 \pm 0.4$ |
| $R^d_{\rm coal}(p_T = 0)$, fm | $2.3 \pm 0.3$ | $2.7 \pm 0.3$ | $2.5 \pm 0.2$ | $2.8 \pm 0.2$ | $3.1 \pm 0.2$ |
| $R^t_{\rm coal}(p_T = 0)$, fm | — | $2.4 \pm 0.2$ | $2.5 \pm 0.2$ | $2.5 \pm 0.2$ | $2.9 \pm 0.2$ |
| $0.22 < y^* < 0.62$ | | | | | |
| $B_2(p_T = 0)/10^3$, GeV$^2$/c$^3$ | $4.07 \pm 1.0$ | $3.56 \pm 0.5$ | $3.0 \pm 0.8$ | $2.06 \pm 0.5$ | $2.67 \pm 0.4$ |
| $B_3(p_T = 0)/10^6$, GeV$^4$/c$^6$ | — | $9.6 \pm 3.0$ | $9.3 \pm 2.9$ | $7.3 \pm 2.7$ | $5.1 \pm 2.3$ |
| $R^d_{\rm coal}(p_T = 0)$, fm | $2.1 \pm 0.2$ | $2.2 \pm 0.2$ | $2.4 \pm 0.2$ | $2.7 \pm 0.2$ | $2.5 \pm 0.2$ |
| $R^t_{\rm coal}(p_T = 0)$, fm | — | $2.2 \pm 0.2$ | $2.3 \pm 0.2$ | $2.4 \pm 0.2$ | $2.5 \pm 0.2$ |

**Table 4.** Coalescence parameters $B_2(p_T = 0)$ and $B_3(p_T = 0)$ extrapolated to $p_T = 0$ using an exponential fit to $B_2(p_T)$ and $B_3(p_T)$; coalescence radii $R^d_{\rm coal}(p_T = 0)$ and $R^t_{\rm coal}(p_T = 0)$ evaluated from the $B_2(p_T = 0)$ and $B_3(p_T = 0)$ values for deuterons and tritons produced in the rapidity ranges $-0.18 < y^* < 0.22$ and $0.22 < y^* < 0.62$ in Ar+A interactions with centrality 0–40%. The quoted errors are the quadratic sums of the statistical and systematic uncertainties.

interactions with centrality 0–40% are consistent with the general trend of decreasing $B_2$ and $B_3$ values with increasing collision energy of central interactions of heavy nuclei. The $B_2$ and $B_3$ values are inversely related to the coalescence radius $R_{\rm coal}$, which is closely related to the LCMS femtoscopic radii of the source $R_{\rm out}$, $R_{\rm side}$, $R_{\rm long} = R_{\parallel}$ with $R_{\rm out}(p_T = 0) = R_{\rm side}(p_T = 0) = R_{\perp}$ [22]. On the basis of eq. (8.2) at $p_T = 0$, one can define $R_{\rm coal} = \sqrt[3]{R_{\parallel} R^2_{\perp}}$ and calculate it from the $B_2(p_T = 0)$ and $B_3(p_T = 0)$ values of deuterons and tritons. In the calculations, the $C_d$ and $C_t$ factors from [56] are scaled according to the mass of the colliding systems to account for the suppression related to the increased effective volume due to the finite deuteron and triton radii, see eq. (4.12) in ref. [22]. The resulting values are in the range of 0.55–0.61 and 0.51–0.58 for $C_d$ and $C_t$, respectively. The results for $R_{\rm coal}$ are also given in table 4.

The coalescence source radii for deuterons and tritons produced in Ar+Al, Cu, Sn and Pb interactions with centrality 0–40% are consistent within the uncertainties. The BM@N values for the coalescence radii averaged for Ar+Al, Cu, Sn and Pb interactions are compared in figure 16 with results obtained at higher energies and for larger collision systems as compiled in ref. [44]. A weak increase of the coalescence radii as a function of the center-of-mass energy in the nucleon-nucleon system is seen in figure 16. One can conclude that the BM@N results reported here are consistent with no or weak dependence of $R_{\rm coal}$ on the target size within the measurement uncertainties.

## 9 Baryon rapidity distributions, stopping and rapidity loss in Ar+A

The total baryon number at a given rapidity in Ar+A collisions at NICA/BM@N energies is basically determined by the nucleons and the light nuclei ($d$, $t$, $^3$He). According to the



JHEP08(2025)095

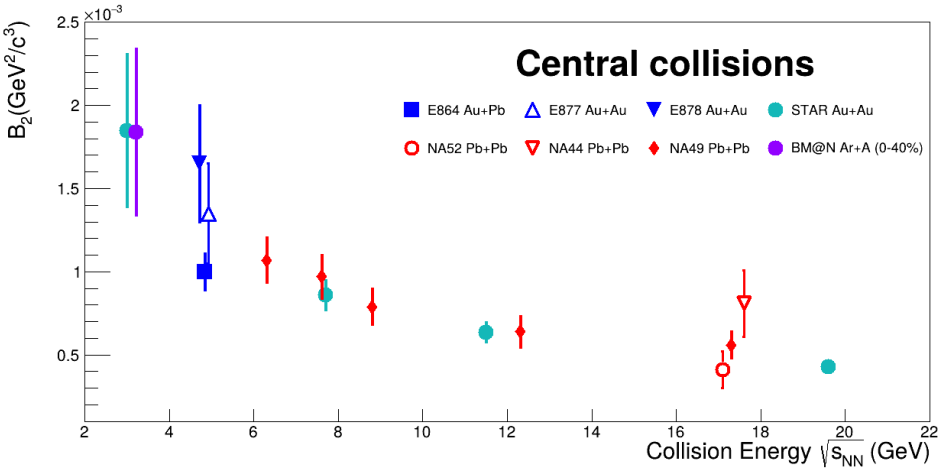


(a)

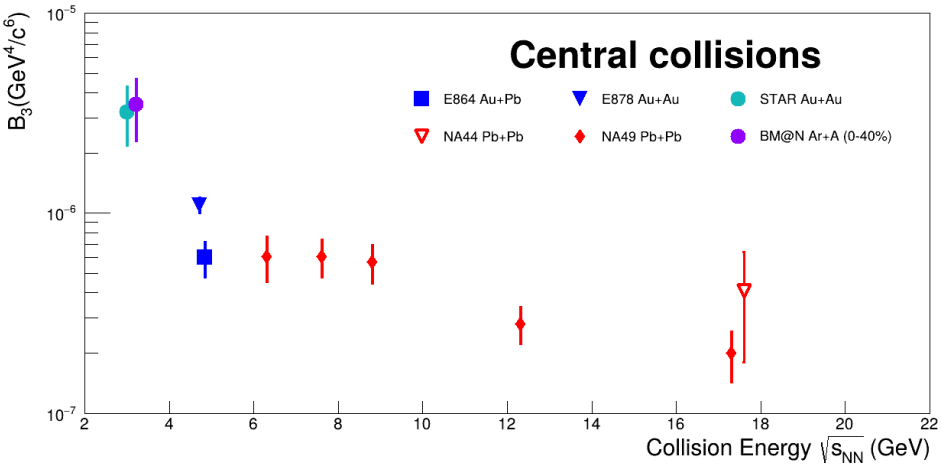


(b)

**Figure 15.** Coalescence parameters $B_2(p_T = 0)$ (a) and $B_3(p_T = 0)$ (b) for deuterons and tritons as functions of the nucleon-nucleon center-of-mass energy. The BM@N result is the weighted average value calculated in the rapidity range $-0.18 < y^* < 0.22$ for Ar+Al, Cu, Sn and Pb interactions with centrality 0–40%.

results on the rapidity spectra of protons and light nuclei presented in section 7, the number of nucleons bound in clusters contributes to the total number of baryons up to about 15% and 25% in central Ar+C and Ar+Pb reactions, respectively. To obtain the baryon rapidity distribution, we add up the baryon number of the measured protons, deuterons and tritons in each rapidity bin. The obtained distribution is then corrected for unmeasured baryons: neutrons, hyperons and $^3$He nuclei. Calculations with the PHQMD and UrQMD models indicate that for all collision systems, the $n/p$ ratio is about 1.1 in the forward hemisphere, varying slowly with rapidity and then increasing abruptly to $\approx 1.22$ (the $n/p$ ratio in the projectile Ar nucleus) at the beam rapidity. We use these model predictions to estimate the yield of neutrons $n$; furthermore, we assume that the $t/^3$He ratio is equal to $n/p$. Hyperons contribute less than 2% to the total baryon number according to the PHQMD and UrQMD [65] models and are thus neglected. The total number of baryons $B$ in a



JHEP08(2025)095

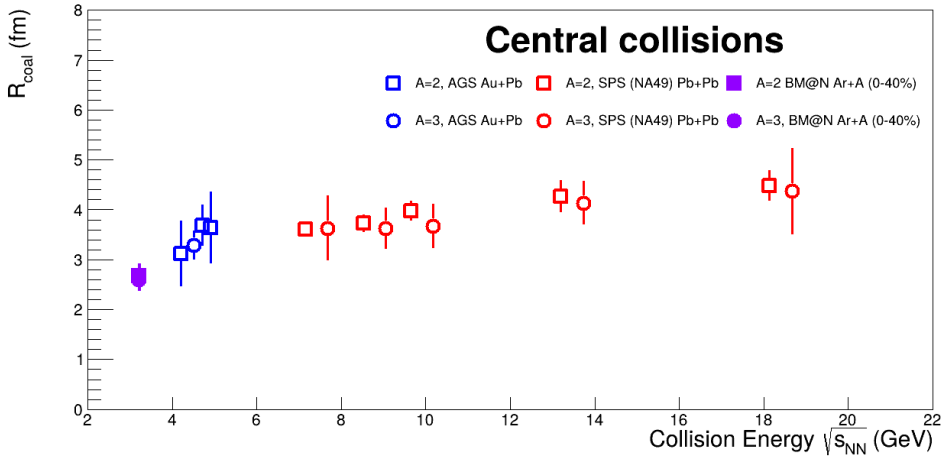


**Figure 16.** Coalescence radii $R_{\rm coal}$ for deuterons and tritons as a function of the nucleon-nucleon center-of-mass energy. The BM@N result is the weighted average value calculated in the rapidity range $-0.18 < y^* < 0.22$ for Ar+Al, Cu, Sn and Pb interactions with centrality 0–40%.

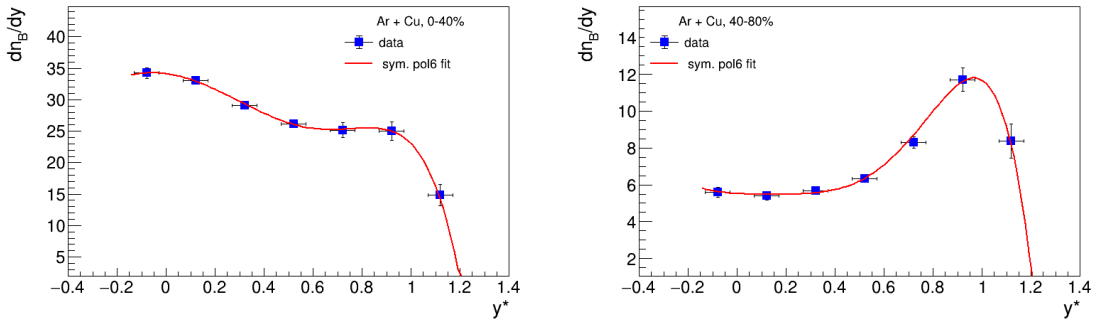


**Figure 17.** Left: rapidity distribution of baryons in 0–40% central Ar+Cu collisions. The measurements are shown by points, whereas the solid line represents the results of a fit with a 3$^{\rm rd}$ order polynomial in $y^{*2}$. Right: same, but for 40–80% central Ar+Cu collisions.

rapidity bin is then calculated as

$$B = p + n + 2 \cdot d + 5.7 \cdot t,$$

where the coefficient in front of $t$ is 5.7. It is calculated as the sum of 3 for tritons and 3/1.1 for $^3$He. The resulting baryon rapidity distributions for Ar+Cu collisions are shown in figure 17 as a function of the rapidity in the center-of-mass system $y^*$: the left panel shows the results for 0–40% central collisions, and the right one is for 40–80% central collisions. A large difference in the shapes of the d$n$/d$y$ distributions is observed as more baryons are transported to midrapidity in the more central collisions. In order to describe those shapes, the data were fitted by a 3$^{\rm rd}$ order polynomial in $y^{*2}$, as suggested in ref. [63]. The results of the fit are shown in figure 17 by solid line curves.

The average rapidity loss is calculated (below $y = y^*$) as:

$$\langle \delta y \rangle = y_b - \langle y \rangle, \tag{9.1}$$



JHEP08(2025)095

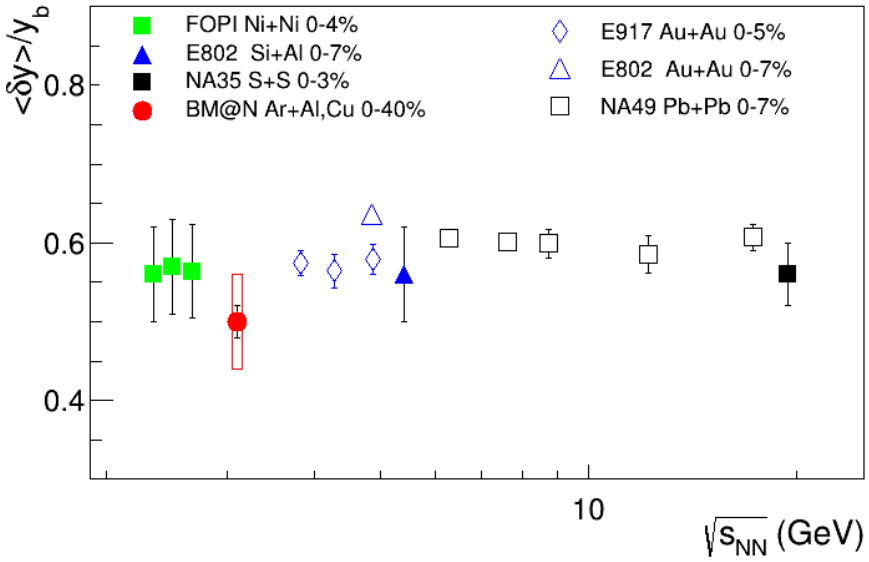


**Figure 18.** The excitation function of the scaled average rapidity loss $\langle \delta y \rangle / y_b$ in nucleus-nucleus collisions. Medium-size colliding systems [64, 66, 67] are drawn by solid symbols, while heavy systems [64, 68, 69] are shown by open ones. Centrality intervals are indicated in the legends. The BM@N data point is the average of Ar+Al and Ar+Cu results, its systematic error is shown by the box.

where $y_b = 1.08$ is the rapidity of the projectile in the center-of-mass system, and the average rapidity:

$$\langle y \rangle = \int_0^{y_b} y \frac{dn}{dy} dy \Big/ \int_0^{y_b} \frac{dn}{dy} dy \,. \tag{9.2}$$

This equation refers to net-baryons, i.e. baryons minus antibaryons. At NICA energies, however, the production of antibaryons is so rare that the difference between baryons and net-baryons is negligible.

The $\langle \delta y \rangle$ values for 0–40% central and 40–80% central Ar+A collisions are listed in table 5. A clear trend is observed: $\langle \delta y \rangle$ increases with the target mass and with collision centrality. This behavior is expected because the probability of multiple interactions in the projectile-target overlap region also rises with the centrality and target mass. The quoted (statistical) uncertainties are the standard errors of the mean $\langle y \rangle$ calculated from the data points within the rapidity range $[0, y_b]$. The systematic error of the rapidity loss values comes from the uncertainty in the fitting procedure used to describe the baryon rapidity spectra. This uncertainty is taken as the difference between the total baryon number estimated from the fit function and the one obtained from the data points. It varies from 7% to 12%.

The energy dependence of the scaled average rapidity shift $\langle \delta y \rangle / y_b$ in nucleus-nucleus collisions as a function of $\sqrt{s_{\rm NN}}$ is shown in figure 18. The average of the BM@N results obtained in Ar+Al and Ar+Cu collisions is shown together with results from medium-size almost symmetric colliding systems from [64, 66, 67] (solid symbols) and those from heavy colliding systems [64, 68, 69] (open symbols). The corresponding centrality intervals are



JHEP08(2025)095

| | Ar+C | Ar+Al | Ar+Cu | Ar+Sn | Ar+Pb |
|---|---|---|---|---|---|
| 0–40% | 0.42 ± 0.04 | 0.50 ± 0.03 | 0.58 ± 0.02 | 0.63 ± 0.02 | 0.65 ± 0.02 |
| 40–80% | 0.38 ± 0.04 | 0.41 ± 0.04 | 0.45 ± 0.03 | 0.47 ± 0.03 | 0.48 ± 0.04 |

**Table 5.** The average rapidity loss $\langle \delta y \rangle$ in Ar+A reactions. The quoted uncertainties are statistical errors.

indicated in the legends. As one can see, the scaled rapidity loss does not vary significantly over a broad energy range.

## 10 Particle ratios

The rapidity and centrality dependence of the deuteron-to-proton ratio $R_{dp}$ in Ar+A collisions at 3.2 A GeV ($\sqrt{s_{\rm NN}} = 3.1$ GeV) is presented in figure 19(a)–19(e). Collisions with centrality 0–40% central and 40–80% are represented by solid and open symbols, respectively. As one can see, $R_{dp}$ rises strongly from midrapidity to the beam rapidity in more peripheral collisions. The same trend is observed in 0–40% central Ar+C collisions. In contrast, in 0–40% central collisions of argon nuclei with aluminum or heavier targets, $R_{dp}$ indicates a plateau-like behavior near midrapidity followed by an increase toward the beam rapidity region. The plateau region for $R_{dp}$ increases gradually with the target mass number covering almost all the measured rapidity range in Ar+Pb collisions.

The midrapidity $R_{dp}$ values from Ar+A collisions with centrality 0–40% and 40–80% as functions of the midrapidity baryon density $\mathrm{d}n_B/\mathrm{d}y$ (obtained from the fits of figure 17) are presented in figure 19(f). As can be seen, $R_{dp}$ increases steadily for low values of $\mathrm{d}n_B/\mathrm{d}y$ and then levels off at higher values.

For a system in chemical equilibrium and a size substantially larger than the deuteron radius, the ratio of the invariant yield of deuterons to the one of protons can be related to the average proton phase-space density at freeze-out $\langle f_p \rangle$ as

$$\langle f_p \rangle = \frac{R_{pn}}{3} \frac{E_d \frac{d^3 N_d}{d^3 P}}{E_p \frac{d^3 N_p}{d^3 p}}, \tag{10.1}$$

where $R_{pn}$ is the proton-to-neutron ratio, $P = 2p$, and the factor of 3 accounts for the particle spins [13]. The $\langle f_p \rangle$ value depends on the strength of the nuclear stopping in the reaction as well as on the outward flow effects.

The $p_T$-dependence of the average proton phase-space density is shown in the left panel of figure 20. Here, the ratio of deuterons to protons is obtained in the rapidity range $0.02 < y^* < 0.42$ and at three $p_T/A$ values: 0.15, 0.3, and 0.45 GeV/c. The $\langle f_p \rangle$ values are calculated according to eq. (10.1). The values of the $R_{pn}$ ratio in the chosen phase-space region were taken from the UrQMD model. As one can see, $\langle f_p \rangle$ decreases with $p_T$ in all reaction systems. Such a trend is indeed expected for a thermal source at a low phase-space density ($f_p \ll 1$), where $\langle f_p \rangle$ follows a Boltzmann distribution and decreases exponentially with $p_T$ [70]. The dashed lines in figure 20 show fits by the exponential function const. $\cdot \exp(-p_T/p_{T0})$ for $\langle f_p \rangle$ from Ar+C and Ar+Pb reactions with $p_{T0}$ as the inverse



JHEP08(2025)095

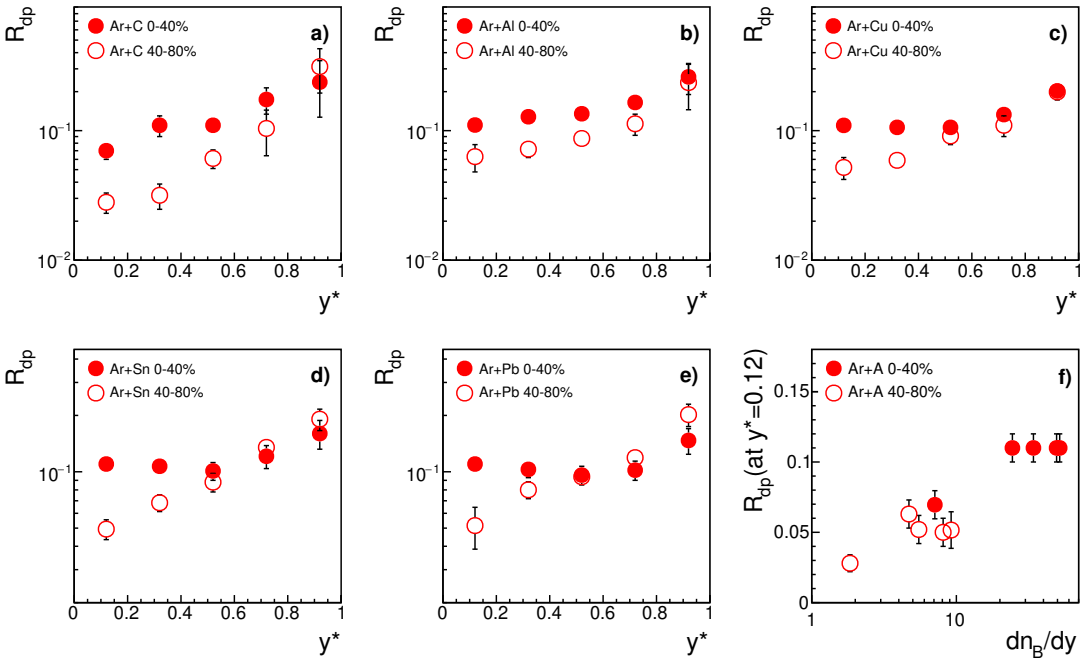


**Figure 19.** $R_{dp}$ as a function of center-of-mass rapidity $y^*$ in Ar+C (a), Ar+Al (b), Ar+Cu (c), Ar+Sn (d), and Ar+Pb (e) collisions. Results for collisions with centrality of 0–40% and 40–80% are shown by solid and open symbols, respectively. Panel (f): midrapidity $R_{dp}$ as a function of midrapidity baryon density $\mathrm{d}n_B/\mathrm{d}y$ in Ar+A collisions.

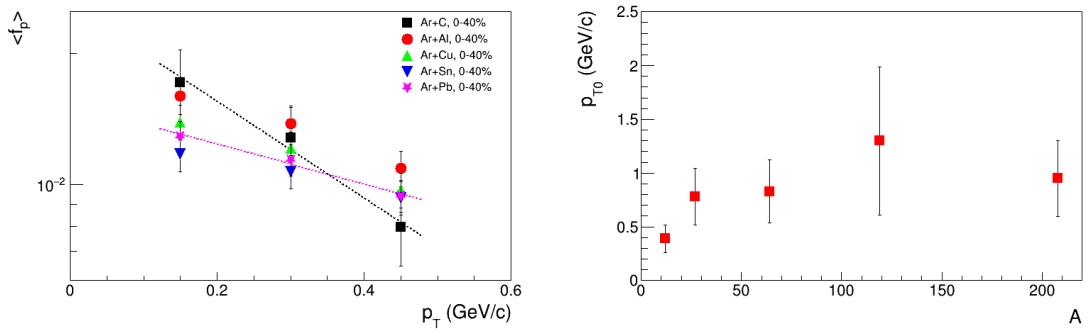


**Figure 20.** Left: average proton phase-space density for 0–40% central Ar+A collisions as a function of $p_T$ within the rapidity range $0.02 < y^* < 0.42$. Dashed lines show fits to exponent (see text for details). Right: the inverse slope parameter $p_{T0}$ of the $p_T$-dependence of $\langle f_p \rangle$ as a function of the target mass number.

slope parameter. It is known that the presence of outward flow in the system makes $f(p_T)$ flatter as the radial velocity increases [71]. The right panel of figure 20 shows the system-size dependence of the slope parameter $p_{T0}$ of the $p_T$-dependence for $\langle f_p \rangle$. As one can see, this dependence is, indeed, correlated with the results on the radial velocity presented in table 3: i.e., weak radial expansion in Ar+C and approximately the same strength of collective radial flow in Ar+Al, Cu, Sn and Pb.

It was identified long time ago that the nuclear cluster abundances and the entropy value attained in the collisions are related. According to an early investigations [72], in a mixture



JHEP08(2025)095

of nucleons and deuterons in thermal and chemical equilibrium, the entropy per nucleon $S_N/A$ can be deduced from the deuteron-to-proton ratio $R_{dp}$ as

$$\frac{S_N}{A} = 3.945 - \ln R_{dp} - \frac{1.25 R_{dp}}{1 + R_{dp}}. \tag{10.2}$$

Furthermore, as the collision energy increases, the contribution of mesons $S_\pi$ to the total entropy becomes important. Following [73], the entropy of pions per nucleon can be estimated by

$$\frac{S_\pi}{A} = 4.1 \frac{N_\pi}{N_N}, \tag{10.3}$$

where $N_N = N_p + N_n$ is the total number of nucleons.

We thus calculated the total entropy $S/A$ near midrapidity as the sum of the nucleon and pion entropy contributions according to eqs. (10.2) and (10.3). To estimate $S_\pi$, we used the recently published BM@N results on positively charged pions [8], while the contribution of $\pi^-$, $\pi^0$, and neutrons was obtained from the UrQMD model. We found that the contribution of pions to the total entropy does not exceed 25% in Ar+A collisions at NICA energies. Finally, $S/A$ is found to be 10.3, 7.8, 7.8, 7.9, and 7.9 in central Ar+C, Ar+Al, Ar+Cu, Ar+Sn, and Ar+Pb, respectively. The estimated uncertainty in $S/A$ is about 15%. In figure 21 the energy dependence of $S/A$ in central heavy-ion collisions is presented. This compilation includes data from experiments that have published numerical values for the midrapidity yields of charged pions, protons, and light nuclei [44, 66, 74–78]. The BM@N "saturation" $S/A$-value of 7.9 is also shown in this figure. As can be seen, the total entropy increases steadily with collision energy.

It has been established experimentally that the cluster production yields scaled by the spin degeneracy factor (2J+1) decrease exponentially with the atomic mass number $A$ [44, 57]. As an example, $\mathrm{d}n/\mathrm{d}y/(2\mathrm{J}+1)$ at midrapidity for $p$, $d$, $t$ as a function of $A$ from 0–40% central Ar+Sn collisions are preseneted in figure 22 (left panel). The particle rapidity density values are extracted from the fits of figure 7. The $A$-dependence of the yields was fitted to a form:

$$\frac{dn}{dy}(A) = \mathrm{const.}/p^{A-1}, \tag{10.4}$$

where the parameter $p$ ('penalty factor') determines the penalty for adding one extra nucleon to the system.

The $p$-factors from central Ar+A collisions are shown in figure 22 (right panel) as a function of the midrapidity baryon rapidity density. The errors are the statistical errors obtained from the fit to eq. (10.4).

Recently, the STAR experiment reported measurements of the compound yield ratio $R_{ptd} = N_p N_t / N_d^2$ of protons ($N_p$) and tritons ($N_t$) to deuterons ($N_d$) [61]. Coalescence models predict [79] that a non-monotonic behavior of the ratio as a function of the system size or collision energy is a signature of the neutron density fluctuations $\Delta n$: $R_{ptd} \approx g(1 + \Delta n)$ with a color factor $g \simeq 0.29$. Following this argument, $R_{ptd}$ is a promising observable to search for the critical point and/or a first-order phase transition in heavy-ion collisions [80].



JHEP08(2025)095

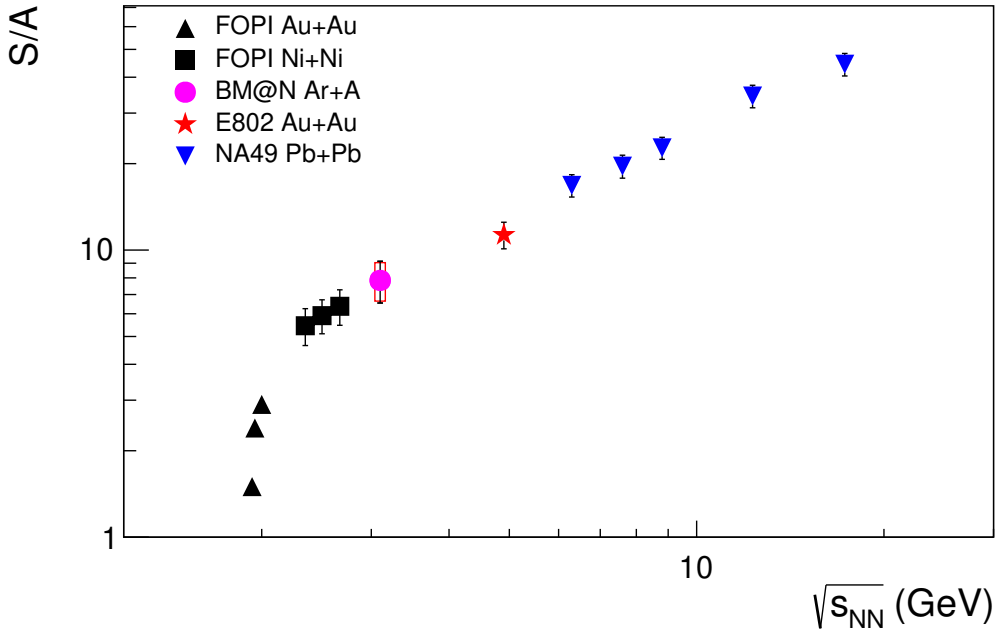


**Figure 21.** The excitation function of the entropy per baryon $S/A$ from SIS/FOPI [66, 74], AGS/E802 [75], SPS/NA49 [44, 76–78] and NICA/BM@N (this study).

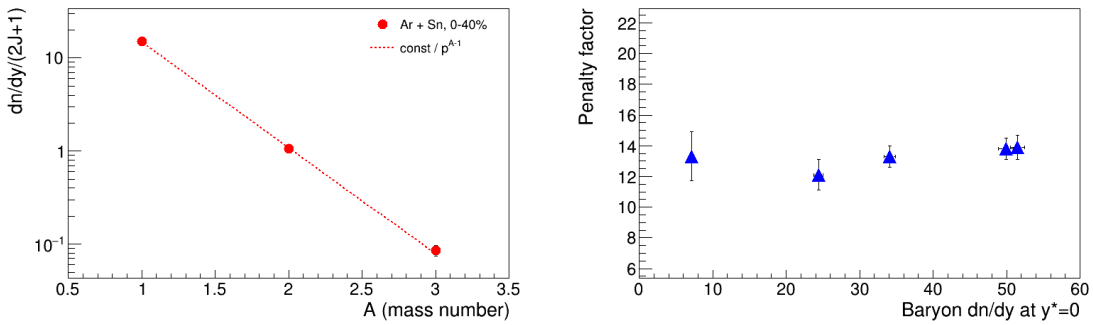


**Figure 22.** Left: midrapidity d$n$/d$y$/(2J+1) for $p$, $d$, $t$ from central Ar+Sn collisions. The dashed line is a fit to eq. (10.4). Right: penalty factor from central Ar+A collisions versus baryon rapidity density at midrapidity.

In coalescence models, the compound yield ratio should increase as the size of the system decreases. Indeed, this effect is observed by the STAR experiment [62].

To evaluate the $R_{ptd}$ ratio, mean values of the $dN/dy$ distributions for protons, deuterons and tritons are calculated in two rapidity ranges: $0.9 < y < 1.3$ ($-0.18 < y^* < 0.22$) and $1.3 < y < 1.7$ ($0.22 < y^* < 0.62$). The results are given in table 6 for argon-nucleus interactions with centrality 0–40%.

No significant variation of the $N_p N_t / N_d^2$ values is observed with the various targets. Taking the differences as systematic uncertainties, the weighted average value of the compound ratio is estimated to be $0.59 \pm 0.065$ for $-0.18 < y^* < 0.22$ and $0.46 \pm 0.10$ for $0.22 < y^* < 0.62$, where the uncertainty is the quadratic sum of the statistical and systematic uncertainties. Within the uncertainties, there is no strong dependence of the $R_{ptd}$ ratio on rapidity in the



JHEP08(2025)095

| | Ar+C | Ar+Al | Ar+Cu | Ar+Sn | Ar+Pb |
|---|---|---|---|---|---|
| $N_pN_t/N_d^2$ $(-0.18 < y^* < 0.22)$ | $0.52 \pm 0.18$ | $0.53 \pm 0.10$ | $0.66 \pm 0.16$ | $0.68 \pm 0.12$ | $0.57 \pm 0.11$ |
| $N_pN_t/N_d^2$ $(0.22 < y^* < 0.62)$ | — | $0.40 \pm 0.07$ | $0.60 \pm 0.08$ | $0.50 \pm 0.08$ | $0.51 \pm 0.12$ |

**Table 6.** $N_pN_t/N_d^2$ values evaluated from the mean $dN/dy$ values of protons, deuterons and tritons over the rapidity range $-0.18 < y^* < 0.22$ and $0.22 < y^* < 0.62$ in Ar+A interactions with centrality 0–40%. The quoted errors are the quadratic sums of the statistical and systematic uncertainties.

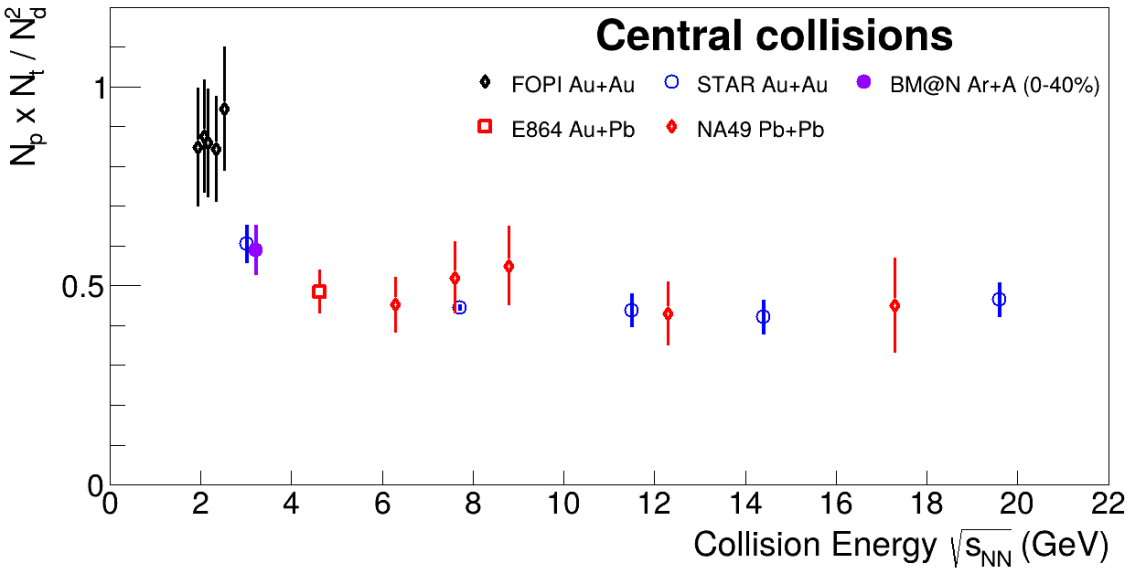


**Figure 23.** Compound yield ratio $N_p \cdot N_t/N_d^2$ of protons ($N_p$) and tritons ($N_t$) to deuterons ($N_d^2$) as a function of the center-of-mass energy of nucleus-nucleus interactions. The BM@N result represents the weighted average value in the rapidity range $-0.18 < y^* < 0.22$ calculated for Ar+Al, Cu, Sn and Pb interactions with centrality 0–40%.

measured rapidity range. The BM@N value for $R_{ptd}$ for $-0.18 < y^* < 0.22$ is compared in figure 23 with the measurements of other experiments. The BM@N result lays between the values of 0.8–1.0 derived by the FOPI experiment (impact parameter $b_0 < 0.15$) [45] at lower energies and the values of 0.4–0.5 obtained by the E864 (0–10% central) [57], STAR (0–10% central) [61, 62] and NA49 (0–7% central) [44] experiments at higher CM energies from 4.3 to 18 GeV. The BM@N value for $R_{ptd}$ is consistent with the STAR Au+Au result measured in the fixed target mode at $\sqrt{s_{\mathrm{NN}}}$ of 3 GeV [41].

## 11 Conclusions

The first results of the BM@N experiment are presented on the proton, deuteron and triton yields and their ratios in argon-nucleus interactions at the beam kinetic energy of 3.2 A GeV. They are compared with the DCM-SMM and PHQMD models and with previously published results of other experiments.



JHEP08(2025)095

The transverse mass $m_T$ spectra are measured and the mean transverse kinetic energy $\langle E_T \rangle = \langle m_T \rangle - m$ are presented for more central 0–40% events as functions of the rapidity $y$ and mass $m$ of the nuclear fragment. The $\langle E_T \rangle$ values are found to depend linearly on the mass $m$. The source temperature at kinetic freeze-out and the average radial velocity are extracted within the Blast-Wave model.

The rapidity density $dN/dy$ of protons, deuterons and tritons are presented for the whole $p_T$ range in two centrality ranges. The DCM-SMM and PHQMD models reproduce the shapes of the spectra but underestimate the deuteron yields by factors of about 3 and 2, respectively. The triton yields predicted by the models are below the experimental data by a factor of about 5.

The average rapidity loss $\langle \delta y \rangle$ increases with the target mass and with the collision centrality. In contrast, the rapidity loss scaled to the beam rapidity $\langle \delta y \rangle / y_b$ in almost symmetric heavy-ion collisions does not vary significantly over a broad energy range.

The ratio of deuterons to protons $R_{dp}$ rises in peripheral collisions and levels off in central ones, possibly indicating a saturation of the nucleon phase-space density at freeze-out. The entropy per baryon $S/A$ was estimated to be $S/A \approx 8$ nicely fitting in the trend of the $S/A$ energy dependence established from other experimental results.

The proton, deuteron and triton yields are used to calculate the coalescence parameters $B_2$ and $B_3$ for deuterons and tritons. Consistent coalescence radii are extracted from $B_2$ and $B_3$ values extrapolated to $p_T = 0$. They are slightly lower compared with the results of experiments at higher energies in agreement with a weak increase of the coalescence radii with increasing collision energy.

The compound yield ratio $N_p N_t / N_d^2$ of protons and tritons to deuterons is evaluated and compared with other measurements at lower and higher energies. The results follow the general trend of decreasing values of $B_2$, $B_3$ and $N_p N_t / N_d^2$ ratio with increasing energy.

## Acknowledgments

The BM@N collaboration acknowledges the efforts of the staff of the accelerator division of the Laboratory of High Energy Physics at JINR that made this experiment possible. The BM@N collaboration acknowledges support of the HybriLIT of JINR for the provided computational resources. The research has been supported by the Ministry of Science and Higher Education of the Russian Federation, Project "New Phenomena in Particle Physics and the Early Universe" No. FSWU-2023-0073 and by the Science Committee of the Ministry of Science and Higher Education of the Republic of Kazakhstan (Grant No. AP23487706).

**Data Availability Statement.** This article has no associated data or the data will not be deposited.

**Code Availability Statement.** This article has no associated code or the code will not be deposited.





JHEP08(2025)095

## References


[1] B. Friman, W. Nörenberg and V.D. Toneev, *The Quark condensate in relativistic nucleus-nucleus collisions*, *Eur. Phys. J. A* **3** (1998) 165 [nucl-th/9711065] [INSPIRE].

[2] J. Randrup and J. Cleymans, *Maximum freeze-out baryon density in nuclear collisions*, *Phys. Rev. C* **74** (2006) 047901 [hep-ph/0607065] [INSPIRE].

[3] C. Fuchs, *Kaon production in heavy ion reactions at intermediate energies*, *Prog. Part. Nucl. Phys.* **56** (2006) 1 [nucl-th/0507017] [INSPIRE].

[4] D. Blaschke et al., *Topical issue on Exploring Strongly Interacting Matter at High Densities — NICA White Paper*, *Eur. Phys. J. A* **52** (2016) 267.

[5] T.O. Ablyazimov et al., *Study of Strange Matter Production in Heavy-Ion Collisions at the Nuclotron*, BM@N Conceptual Design Report (2013), http://nica.jinr.ru/files/BM@N/BMN_CDR.pdf.

[6] M. Kapishin, *Studies of baryonic matter at the BM@N experiment (JINR)*, *Nucl. Phys. A* **982** (2019) 967 [INSPIRE].

[7] BM@N collaboration, *BM@N First Results*, in the proceedings of the *18th International Conference on Strangeness in Quark Matter (SQM 2019)*, Bari, Italy, 10–15 June 2019, *Springer Proceedings in Physics* **250**, Springer, Cham, Switzerland (2020), pp. 21–27 [DOI:10.1007/978-3-030-53448-6_3] [INSPIRE].

[8] BM@N collaboration, *Production of $\pi^+$ and $K^+$ mesons in argon-nucleus interactions at 3.2 A GeV*, *JHEP* **07** (2023) 174 [arXiv:2303.16243] [INSPIRE].

[9] W. Busza and A.S. Goldhaber, *Nuclear Stopping Power*, *Phys. Lett. B* **139** (1984) 235 [INSPIRE].

[10] G.C. Rossi and G. Veneziano, *I. Theoretical aspects of baryonium physics*, *Phys. Rep.* **63** (1980) 153.

[11] A. Capella and B.Z. Kopeliovich, *Novel mechanism of nucleon stopping in heavy ion collisions*, *Phys. Lett. B* **381** (1996) 325 [hep-ph/9603279] [INSPIRE].

[12] D. Kharzeev, *Can gluons trace baryon number?*, *Phys. Lett. B* **378** (1996) 238 [nucl-th/9602027] [INSPIRE].

[13] M. Murray and B. Holzer, *(Anti-)proton and pion source sizes and phase space densities in heavy ion collisions*, *Phys. Rev. C* **63** (2001) 054901 [nucl-ex/0008006] [INSPIRE].

[14] A. Andronic, P. Braun-Munzinger and J. Stachel, *Thermal hadron production in relativistic nuclear collisions: The Hadron mass spectrum, the horn, and the QCD phase transition*, *Phys. Lett. B* **673** (2009) 142 [*Erratum ibid.* **678** (2009) 516] [arXiv:0812.1186] [INSPIRE].

[15] E864 collaboration, *Mass dependence of light nucleus production in ultrarelativistic heavy ion collisions*, *Phys. Rev. Lett.* **83** (1999) 5431 [nucl-ex/9907002] [INSPIRE].

[16] G. Bertsch and J. Cugnon, *Entropy production in high energy collisions*, *Phys. Rev. C* **24** (1981) 2514 [INSPIRE].

[17] J. Kapusta, *Viscous heating of expanding fireballs*, *Phys. Rev. C* **24** (1981) 2545 [INSPIRE].

[18] S.T. Butler and C.A. Pearson, *Deuterons from High-Energy Proton Bombardment of Matter*, *Phys. Rev.* **129** (1963) 836 [INSPIRE].

[19] A. Schwarzschild and Č. Zupančič, *Production of Tritons, Deuterons, Nucleons, and Mesons by 30 GeV Protons on A1, Be, and Fe Targets*, *Phys. Rev.* **129** (1963) 854 [INSPIRE].

[20] S. Mrówczyński, *On the neutron proton correlations and deuteron production*, *Phys. Lett. B* **277** (1992) 43 [INSPIRE].




JHEP08(2025)095

[21] H. Sato and K. Yazaki, *On the coalescence model for high-energy nuclear reactions*, *Phys. Lett. B* **98** (1981) 153 [INSPIRE].

[22] R. Scheibl and U. Heinz, *Coalescence and flow in ultrarelativistic heavy ion collisions*, *Phys. Rev. C* **59** (1999) 1585 [nucl-th/9809092] [INSPIRE].

[23] N. Amelin, K. Gudima and V. Toneev, *Ultrarelativistic nucleus-nucleus collisions within a dynamical model of independent quark-gluon strings* (in Russian), *Sov. J. Nucl. Phys.* **51** (1990) 1093 [INSPIRE].

[24] M. Baznat, A. Botvina, G. Musulmanbekov, V. Toneev and V. Zhezher, *Monte-Carlo Generator of Heavy Ion Collisions DCM-SMM*, *Phys. Part. Nucl. Lett.* **17** (2020) 303 [arXiv:1912.09277] [INSPIRE].

[25] J. Aichelin, E. Bratkovskaya et al., *Parton-hadron-quantum-molecular dynamics: A novel microscopic n-body transport approach for heavy-ion collisions, dynamical cluster formation, and hypernuclei production*, *Phys. Rev. C* **101** (2020) 044905 [arXiv:1907.03860] [INSPIRE].

[26] M.N. Kapishin et al., *Studies of Baryonic Matter at the Nuclotron (BM@N)*, JINR (2010), https://bmn.jinr.int/detector/project/BMN_project.pdf.

[27] S. Afanasiev et al., *The BM@N spectrometer at the NICA accelerator complex*, *Nucl. Instrum. Meth. A* **1065** (2024) 169532 [arXiv:2312.17573] [INSPIRE].

[28] D. Baranov et al., *GEM tracking system of the BM@N experiment*, 2017 *JINST* **12** C06041 [INSPIRE].

[29] V. Babkin et al., *Triple-stack multigap resistive plate chamber with strip readout*, *Nucl. Instrum. Meth. A* **824** (2016) 490 [INSPIRE].

[30] V. Babkin et al., *Strip MRPC for the MPD/NICA Time-of-Flight System*, in the proceedings of the *Technology and Instrumentation in Particle Physics 2014 (TIPP2014)*, Amsterdam, Netherlands, 2–6 June 2014, *PoS* **TIPP2014** (2015) 289 [INSPIRE].

[31] N. Kuzmin et al., *High-rate glass MRPC for fixed target experiments at Nuclotron*, *Nucl. Instrum. Meth. A* **916** (2019) 190 [arXiv:1811.08637] [INSPIRE].

[32] K. Alishina et al., *Charged Particle Identification by the Time-of-Flight Method in the BM@N Experiment*, *Phys. Part. Nucl.* **53** (2022) 470 [INSPIRE].

[33] V. Akishina and I. Kisel, *Time-based Cellular Automaton track finder for the CBM experiment*, *J. Phys. Conf. Ser.* **599** (2015) 012024 [INSPIRE].

[34] I. Kisel, *Event reconstruction in the CBM experiment*, *Nucl. Instrum. Meth. A* **566** (2006) 85 [INSPIRE].

[35] R. Brun et al., *GEANT Detector Description and Simulation Tool*, CERN-W5013, Geneva, CERN, Switzerland (1994) [INSPIRE].

[36] https://git.jinr.ru/nica/bmnroot.

[37] V. Plotnikov, L. Kovachev and A. Zinchenko, *Detector Efficiency in the BM@N Experiment in an Argon Run with a Beam Energy of* 3.2 *A GeV at Nuclotron*, *Phys. Part. Nucl. Lett.* **20** (2023) 1392 [INSPIRE].

[38] K. Kanaki, *Study of* $\Lambda$ *hyperon production in C+C collisions at* 2 *A GeV beam energy with the HADES spectrometer*, Ph.D. Thesis, Dresden University of Technology, Dresden, Germany (2007).

[39] N. Angelov et al., *Analysis of Behavior of Cross-section and* $\pi^-$ *Meson Multiplicity at the Interaction of p, d, He, C Relativistic Nuclei With*, *Sov. J. Nucl. Phys.* **33** (1981) 552 [*Yad. Fiz.* **33** (1981) 1046] [JINR-P1-80-473] [INSPIRE].



JHEP08(2025)095

[40] BM@N, https://bmn.jinr.int/wp-content/uploads/2025/02/Tabulated-results-from-the-paper.pdf.

[41] STAR collaboration, *Production of protons and light nuclei in Au+Au collisions at* $\sqrt{s_{\rm NN}} = 3$ *GeV with the STAR detector*, *Phys. Rev. C* **110** (2024) 054911 [arXiv:2311.11020] [INSPIRE].

[42] V. Vovchenko et al., *Feeddown contributions from unstable nuclei in relativistic heavy-ion collisions*, *Phys. Lett. B* **809** (2020) 135746 [arXiv:2004.04411] [INSPIRE].

[43] D.R. Tilley, H.R. Weller and G.M. Hale, *Energy levels of light nuclei* $A = 4$, *Nucl. Phys. A* **541** (1992) 1 [INSPIRE].

[44] NA49 collaboration, *Production of deuterium, tritium, and* $^3$*He in central Pb + Pb collisions at* 20 *A*, 30 *A*, 40 *A*, 80 *A, and* 158 *A GeV at the CERN Super Proton Synchrotron*, *Phys. Rev. C* **94** (2016) 044906 [arXiv:1606.04234] [INSPIRE].

[45] FOPI collaboration, *Systematics of central heavy ion collisions in the* 1 *A GeV regime*, *Nucl. Phys. A* **848** (2010) 366 [arXiv:1005.3418] [INSPIRE].

[46] EOS collaboration, *Radial flow in Au + Au collisions at* $E = (0.25 - 1.15)$ *A Gev*, *Phys. Rev. Lett.* **75** (1995) 2662 [nucl-ex/9502001] [INSPIRE].

[47] L. Kumar, *Systematics of Kinetic Freeze-out Properties in High Energy Collisions from STAR*, *Nucl. Phys. A* **931** (2014) 1114 [arXiv:1408.4209] [INSPIRE].

[48] STAR collaboration, *Bulk Properties of the Medium Produced in Relativistic Heavy-Ion Collisions from the Beam Energy Scan Program*, *Phys. Rev. C* **96** (2017) 044904 [arXiv:1701.07065] [INSPIRE].

[49] H. Liu, *Measurement of Light-nuclei Production in Heavy-ion Collisions by the STAR Experiment*, *Acta Phys. Pol. B Proc. Suppl.* **16** (2023) 1-A148 [arXiv:2208.04650].

[50] E. Schnedermann, J. Sollfrank and U.W. Heinz, *Thermal phenomenology of hadrons from* 200 *A GeV S+S collisions*, *Phys. Rev. C* **48** (1993) 2462 [nucl-th/9307020] [INSPIRE].

[51] A.Z. Mekjian, *Thermodynamic Model for Composite Particle Emission in Relativistic Heavy Ion Collisions*, *Phys. Rev. Lett.* **38** (1977) 640 [INSPIRE].

[52] A.Z. Mekjian, *Explosive nucleosynthesis, equilibrium thermodynamics, and relativistic heavy-ion collisions*, *Phys. Rev. C* **17** (1978) 1051 [INSPIRE].

[53] A.Z. Mekjian, *Statistical Thermodynamics of Relativistic Heavy Ion Collisions*, *Nucl. Phys. A* **312** (1978) 491 [INSPIRE].

[54] J.I. Kapusta, *Mechanisms for deuteron production in relativistic nuclear collisions*, *Phys. Rev. C* **21** (1980) 1301 [INSPIRE].

[55] K. Nakamura et al., *Review of particle physics*, *J. Phys. G* **37** (2010) 075021 [INSPIRE].

[56] I.G. Bearden et al., *Deuteron and triton production with high energy sulphur and lead beams*, *Eur. Phys. J. C* **23** (2002) 237 [INSPIRE].

[57] E864 collaboration, *Measurements of light nuclei production in* 11.5 *A GeV/c Au + Pb heavy ion collisions*, *Phys. Rev. C* **61** (2000) 064908 [nucl-ex/0003009] [INSPIRE].

[58] E877 collaboration, *Light fragment yields from Au + Au collisions at* 11.5 *A GeV/c*, *Phys. Rev. C* **61** (2000) 044906 [nucl-ex/9906005] [INSPIRE].

[59] E878 collaboration, *Light nuclei production in relativistic Au + nucleus collisions*, *Phys. Rev. C* **58** (1998) 1155 [INSPIRE].

[60] NEWMASS (NA52) collaboration, *Baryon and anti-baryon production in lead-lead collisions at* 158 *A GeV/c*, *Phys. Lett. B* **417** (1998) 202 [INSPIRE].



JHEP08(2025)095

[61] STAR collaboration, *Beam Energy Dependence of Triton Production and Yield Ratio $(N_t \times N_p/N_d^2)$ in Au+Au Collisions at RHIC*, *Phys. Rev. Lett.* **130** (2023) 202301 [arXiv:2209.08058] [INSPIRE].

[62] D. Zhang, *Light Nuclei $(d, t)$ Production in Au + Au Collisions at $\sqrt{s_{\rm NN}} = 7.7$–200 GeV*, *Nucl. Phys. A* **1005** (2021) 121825 [arXiv:2002.10677] [INSPIRE].

[63] BRAHMS collaboration, *Nuclear stopping in Au + Au collisions at $\sqrt{s_{\rm NN}} = 200$ GeV*, *Phys. Rev. Lett.* **93** (2004) 102301 [nucl-ex/0312023] [INSPIRE].

[64] F. Videbaek and O. Hansen, *Baryon rapidity loss and mid-rapidity stacking in high-energy nucleus-nucleus collisions*, *Phys. Rev. C* **52** (1995) 2684 [INSPIRE].

[65] S.A. Bass et al., *Microscopic models for ultrarelativistic heavy ion collisions*, *Prog. Part. Nucl. Phys.* **41** (1998) 255 [nucl-th/9803035] [INSPIRE].

[66] FOPI collaboration, *Stopping and radial flow in central $^{58}Ni$ + $^{58}Ni$ collisions between 1 A and 2 A GeV*, *Phys. Rev. C* **57** (1998) 244 [*Erratum ibid.* **58** (1998) 603] [nucl-ex/9707001] [INSPIRE].

[67] NA35 collaboration, *Charged particle spectra in central S + S collisions at 200 GeV/c per nucleon*, *Phys. Rev. Lett.* **72** (1994) 1419 [INSPIRE].

[68] E917 collaboration, *Baryon rapidity loss in relativistic Au+Au collisions*, *Phys. Rev. Lett.* **86** (2001) 1970 [nucl-ex/0003007] [INSPIRE].

[69] C. Blume, *Centrality and energy dependence of proton, light fragment and hyperon production*, *J. Phys. G* **34** (2007) S951 [nucl-ex/0701042] [INSPIRE].

[70] M.J. Murray, *Kaon phase space density in heavy ion collisions*, *J. Phys. G* **28** (2002) 2069 [nucl-ex/0201006] [INSPIRE].

[71] B. Tomasik and U. Heinz, *Flow effects on the freezeout phase space density in heavy ion collisions*, *Phys. Rev. C* **65** (2002) 031902(R) [nucl-th/0108051] [INSPIRE].

[72] L.P. Csernai and J.I. Kapusta, *Entropy and Cluster Production in Nuclear Collisions*, *Phys. Rep.* **131** (1986) 223 [INSPIRE].

[73] S.Z. Belen'kji and L.D. Landau, *Hydrodynamic Theory of Multiple Formation of Particles*, *Nuovo Cim.* **3S1** (1956) 15 [*Usp. Fiz. Nauk* **56** (1955) 309] [INSPIRE].

[74] FOPI collaboration, *Evidence for collective expansion in light-particle emission following Au+Au collisions at 100, 150 and 250 A MeV*, *Nucl. Phys. A* **586** (1995) 755 [INSPIRE].

[75] E802 collaboration, *Proton and deuteron production in Au + Au reactions at 11.6 A GeV/c*, *Phys. Rev. C* **60** (1999) 064901 [INSPIRE].

[76] NA49 collaboration, *Energy and centrality dependence of deuteron and proton production in Pb + Pb collisions at relativistic energies*, *Phys. Rev. C* **69** (2004) 024902 [INSPIRE].

[77] NA49 collaboration, *Pion and kaon production in central Pb + Pb collisions at 20 A and 30 A GeV: Evidence for the onset of deconfinement*, *Phys. Rev. C* **77** (2008) 024903 [arXiv:0710.0118] [INSPIRE].

[78] NA49 collaboration, *Antideuteron and deuteron production in mid-central Pb+Pb collisions at 158 A GeV*, *Phys. Rev. C* **85** (2012) 044913 [arXiv:1111.2588] [INSPIRE].

[79] K.-J. Sun, L.-W. Chen, C.M. Ko and Z. Xu, *Probing QCD critical fluctuations from light nuclei production in relativistic heavy-ion collisions*, *Phys. Lett. B* **774** (2017) 103 [arXiv:1702.07620] [INSPIRE].

[80] D. Oliinychenko, *Overview of light nuclei production in relativistic heavy-ion collisions*, *Nucl. Phys. A* **1005** (2021) 121754 [arXiv:2003.05476] [INSPIRE].

JHEP08(2025)095